Dynamical importance of the trade wind inversion in suppressing the southeast Pacific ITCZ

Alex O. Gonzalez[1,2], Indrani Ganguly[2], Marissa Osterloh[2], Gregory V. Cesana[3], and Charlotte A. DeMott[4]

[1]Department of Physical Oceanography, Woods Hole Oceanographic Institution
[2]Department of Geological and Atmospheric Sciences, Iowa State University
[3]Center for Climate Systems Research, Columbia University
[4]Department of Atmospheric Science, Colorado State University

Key Points:

- East Pacific ITCZ surface wind convergence is strongly controlled by SST and boundary layer horizontal temperature gradients.
- An idealized model shows SST gradients on their own produce excessive equatorial cold tongue divergence and southern hemisphere convergence.
- The trade wind inversion counteracts SST-driven double ITCZs due to strong longwave cooling at the top of the boundary layer low clouds.

Corresponding author: Alex O. Gonzalez, `alex.gonzalez@whoi.edu`

Abstract

Sea surface temperature (SST) gradients are a primary driver of low-level wind convergence in the Inter-Tropical Convergence Zone (ITCZ) through their hydrostatic relationship to the surface pressure force (PGF). To what extent boundary layer virtual temperature gradients have an effect on ITCZ convergence through their modulation of the surface PGF is not well understood. In this study, we investigate the reasons for the observed northern hemisphere position of the east Pacific ITCZ using a slab boundary layer model (SBLM) driven by different approximations of the surface and boundary layer virtual temperature field within the surface PGF forcing. SBLM simulations using the entire boundary layer virtual temperature profile produce a realistic northern hemisphere ITCZ. However, SST-only simulations produce excessive equatorial divergence and southern hemisphere convergence resulting in a double ITCZ-like structure. Subsequent investigations of virtual temperature gradients highlight the importance of temperature gradients weakening with height more strongly from the equator to 15 degrees south just below the trade wind inversion (TWI). Our interpretation is that the equatorial cold tongue induces relatively high surface pressure and a double ITCZ-like convergence. At the same time, relatively high surface pressure spreads out in the southern hemisphere due to longwave cooling at the top of stratocumulus clouds just below the TWI. Together, the equatorial cold tongue and the TWI/stratocumulus clouds enable a more northern hemisphere dominant ITCZ. Thus, we provide evidence of a dynamical link between double ITCZs and low clouds, which both continue to be problematic in Earth system models.

Plain Language Summary

State-of-the-art climate models have been plagued by biases in the Inter-Tropical Convergence Zone (ITCZ), where the trade winds converge and the world's most intense rainfall occurs. Climate models often produce one ITCZ in each hemisphere, a double ITCZ, when there is nearly always one ITCZ in the northern hemisphere. In this study, we investigate why the ITCZ is nearly always located in the northern hemisphere over the east Pacific Ocean using an idealized model driven by observed southern and northern hemisphere contrasts in: i) sea surface temperature (SST) only and ii) both SST and atmospheric temperature. Experiments driven by only SST contrasts produce a double ITCZ-like structure that is reminiscent of climate model double ITCZ biases. A cold tongue of ocean water on the equator induces relatively high surface pressure and a double ITCZ-like wind convergence. At the same time, relatively high surface pressure spreads out in the southern hemisphere due to cooling at the top of stratocumulus clouds just below a strong temperature inversion. Together, the equatorial cold tongue and stratocumulus clouds enable a more northern hemisphere dominant ITCZ. This study provides a dynamical link between double ITCZs and low clouds, which both continue to be problematic in models.

1 Introduction

The east Pacific Ocean intetropical convergence zone (ITCZ) is highly modulated by variations in the tropical boundary layer winds, which often produce horizontal convergence that is co-located with ITCZ precipitation (Lindzen & Nigam, 1987; Liu & Xie, 2002; Gonzalez et al., 2022). The cause of these boundary layer wind variations is commonly diagnosed through the zonal and meridional momentum budgets (Holton et al., 1971; Mahrt, 1972a, 1972b; Holton, 1975; Lindzen & Nigam, 1987; Tomas et al., 1999; McGauley et al., 2004; Raymond et al., 2006; Sobel & Neelin, 2006; Back & Bretherton, 2009a; Gonzalez & Schubert, 2019; Gonzalez et al., 2022). A leading term in boundary layer momentum budgets is the surface pressure gradient force (PGF), especially in regions where there are strong sea surface temperature (SST) gradients (Lindzen & Nigam, 1987; Back & Bretherton, 2009b; Duffy et al., 2020). The link between SST and surface pressure gradients comes from hydrostatic balance when integrated vertically. In a hydrostatic atmosphere, the surface pressure is determined by the density of the overlying atmospheric column. Therefore, regions with cool SSTs tend to have a higher surface pressure due to a heavier column above and regions with warm SSTs tend to have a a lower surface pressure due to a lighter column above.

Lindzen and Nigam (1987); Back and Bretherton (2009a); Duffy et al. (2020), and Zhou et al. (2020) used hydrostatic balance and a linear mixed layer model (MLM) of Stevens et al. (2001) to quantify how well SST gradients explain large-scale boundary layer winds and convergence in the tropics. One main assumption among these studies is that when taking the vertical integral to solve for the surface pressure gradient, they assume temperature gradients decrease with height in the boundary layer at the same rate everywhere. However, this assumption does not always hold true because of strong changes in lapse rates over wide swaths of tropical to subtropical latitudes, especially where there are low clouds and a trade wind inversion (TWI) at the top of the boundary layer (Klein & Hartmann, 1993; Bretherton et al., 2004; Wood, 2012). The TWI layer, where temperature increases with height, is typically driven by strong longwave radiative cooling at cloud top that is also shifted southward of the near-surface cold anomaly associated with the equatorial cold tongue (Mansbach & Norris, 2007). This implies that temperature gradients above the surface are different from SST gradients, with high surface pressure likely extending further southward because of the effect of the strong longwave cooling associated with low clouds in the southern hemisphere. If this indeed the case, these ideas could help partially explain why surface/boundary layer winds and ITCZ convergence are more accurately diagnosed in the MLM when the surface PGF is estimated using boundary layer virtual temperature gradients (which include TWI effects) than SST gradients alone (Back & Bretherton, 2009a; Duffy et al., 2020). Furthermore, we wonder whether these ideas about localized changes in temperature gradients can help explain the overproduction of double convergence zones over the Atlantic and east Pacific in the SST-driven version of the MLM (Back & Bretherton, 2009a; Duffy et al., 2020; Zhou et al., 2020).

At the same time, it is widely known that ITCZ biases in Earth system models (ESMs) can often be attributed in part to insufficient low cloud production in the southeast Pacific (Mechoso et al., 1995; Woelfle et al., 2019; G. J. Zhang et al., 2019). A dearth of low clouds in ESMs is typically associated with excessive surface insolation, large atmospheric net energy input, and/or insufficient latent heat fluxes (M. H. Zhang et al., 2005; Nam et al., 2012; Cesana & Waliser, 2016; Song & Zhang, 2016; Adam et al., 2018; G. J. Zhang et al., 2019). Of all low clouds, stratocumulus clouds are of particular interest because they have cloud decks that often extend thousands of kilometers horizontally, allowing them to potentially impact the large-scale thermodynamics and dynamics. Stratocumulus clouds form at the base of a very thin ($\mathcal{O}$ (10–100 m)) TWI layer (Haman et al., 2007; Wood, 2012) that is difficult to resolve (Bretherton et al., 2004; Woelfle et al., 2019).

While ITCZ biases can exist in atmosphere-only model simulations (Xiang et al., 2017, 2018), they grow substantially when ocean coupling is employed (Xie & Philander, 1994; Lin, 2007; G. J. Zhang et al., 2019). Moreover, the significance of SST gradients in driving boundary layer winds and convergence is not to be ignored. SST gradients and their anomalies have been critical to understanding the interactions between the atmosphere and ocean by anchoring the theory of wind-evaporation-SST (WES) feedbacks, which are driven by the dynamical and surface latent heat flux response to SST and sea level pressure anomalies (Xie & Philander, 1994; Chelton et al., 2001; Li & Xie, 2014). Recent work by Karnauskas (2022) demonstrated that changes in lower atmospheric stratification, momentum mixing, and surface latent heat fluxes are also important to consider as a negative feedback mechanism that counteracts WES feedbacks (Hayes et al., 1989; Wallace et al., 1989).

In this study, we seek theoretical insight into the importance of both horizontal gradients of SST and boundary layer virtual temperature on boundary layer convergence in the east Pacific. We interrogate hydrostatic balance in reanalyses and develop a set of idealized slab boundary layer model simulations with different surface PGF forcings based on SST versus boundary layer virtual temperature gradients. We aim to highlight the importance of localized, but still large scale, changes in lapse rates, i.e. those associated with the TWI and low clouds, in altering the surface PGF, which is known to be a driver of boundary layer convergence. We deem this the "dynamical" part, however, this is not to be confused with other important dynamical processes, such as the vertical mixing of horizontal momentum.

This paper is organized as follows. Section 2 discusses the use of atmospheric and oceanic fields from reanalyses and low cloud fractions from the Cumulus and Stratocumulus CloudSat-CALIPSO Dataset (CASCCAD). We also derive two formulas, one that decomposes the surface PGF into components from vertically integrated virtual temperature gradients and free tropospheric PGF and the other to decompose virtual temperature gradients into a temperature only part and a covarying moisture and temperature part. The last part of Section 2 describes the four experiments using a nonlinear slab boundary layer model (SBLM) that test different forms of the surface PGF. Section 3 begins by analyzing the surface PGF forcings and SBLM simulation boundary layer wind convergence across the four experiments. The latter part of Section 3 compares the meridional-vertical structure between boundary layer virtual temperature gradients and temperature gradients due solely to SST gradients and ties the differences to localized changes in lapse rates, the TWI, and stratocumulus clouds. Section 4 summarizes the broad-reaching results and discusses the implications within the context of a dynamical link between low clouds, the equatorial cold tongue, and the ITCZ.

2 Methods

2.1 ERA5 Reanalysis

We employ various monthly atmospheric and oceanic fields from the ECMWF's Fifth Re-Analysis (ERA5) at a horizontal resolution of 0.25° for the period of 1979–2020 (Hersbach & coauthors, 2020). All fields are zonally averaged over the east Pacific (90–125°W) using only ocean points after any covarying terms, numerical derivatives, or numerical integrals are computed. For horizontal derivatives, we use central second-order spatial finite difference methods. For vertical integrals, we use the numerical approximation given in Table 1.

2.2 The Cumulus and Stratocumulus CloudSat-CALIPSO Dataset (CASCCAD)

The Cumulus and Stratocumulus CloudSat-CALIPSO Dataset (CASCCAD, Cesana et al. (2019)) distinguishes stratocumulus (Sc), cumulus (Cu), and the transitioning clouds in between, i.e., broken Sc, Cu under Sc and Cu with stratiform outflow, at the orbital level based on morphology (geometrical shape and spatial heterogeneity). The CASCCAD algorithm is utilized on instantaneous profiles of active-sensor CALIPSO-GOCCP (Chepfer et al., 2010) from 2007 through 2016 and CloudSat-CALIPSO GeoProf (Mace & Zhang, 2014) from 2007 through 2010. The results of a case study analysis show that CASCCAD robustly captures Sc, Cu, and transitions between the two regimes, even better than previous satellite data products (Cesana et al., 2019). Thus, CASCCAD represents one of the best currently-available observational constraints on the global scale distribution of Sc, which we will use in this project to study the relationship between the ITCZ, TWI, and Sc clouds over the east Pacific.

With a longer time record and a better horizontal resolution (90 m every 333 m) than CloudSat-CALIPSO GeoProf, CALIPSO-GOCCP CASCCAD makes it possible to detect all fractionated shallow cumulus clouds and to analyze climatological values of Sc and Cu clouds. However, as the lidar penetrates within cloudy layers, the CALIPSO-GOCCP signal eventually attenuates completely for optical thickness greater than 3 to 5. In these instances, i.e., in deep convective clouds or in the storm tracks, the Cloud Profiling Radar (CPR) capability of CloudSat complements cloud profiles beneath the height at which the lidar attenuates, making CloudSat-CALIPSO CASCCAD a better choice than CALIPSO-GOCCP CASCCAD, although the CPR clutter prevents using CloudSat data below 1000 m and its shorter time record.

2.3 Surface Pressure Gradient Force from Hydrostatic Balance

Given that output from ERA5 is on pressure levels, we integrate the horizontal gradient of hydrostatic balance of the form $\frac{\partial \Phi}{\partial (\ln p)} = -R_d T_v$, from the surface pressure p_s to some lower free tropospheric pressure p, arriving at the equation

$$-\frac{1}{\rho_s}\nabla p_s = -\left(\nabla\Phi\right)_{p_s} = R_d \int_p^{p_s} \left(\nabla T_v\right) d\ln p' - \left(\nabla\Phi\right)_p . \tag{1}$$

where ρ_s is the surface density, ∇ is the horizontal gradient operator, $T_v = \left(1 + \frac{R_v}{R_d} q\right) T$ is virtual temperature, R_v is the water vapor air gas constant, R_d is the dry air gas constant, T is temperature, and q is specific humidity. Equation (1) implies that the horizontal surface PGF (note the negative sign in front of $\nabla\Phi$) is driven by: i) horizontal T_v gradients from the surface up until the some pressure level (here we assume where the TWI maximizes, 850 hPa) and ii) the horizontal PGF at TWI level (here 850 hPa). Equation (1) will be numerically integrated using formulas in Table 1 for each of four experiments using an idealized boundary layer model, which will discussed in the next subsection.

Since the form of hydrostatic balance we use involves the role of water vapor through virtual temperature T_v rather than T alone, the role of water vapor on T_v gradients will be diagnosed by decomposing T_v gradients into a T-only part and a part involving the q and T, i.e.,

$$\nabla T_v = \nabla T + \left(\frac{R_v}{Rd} - 1\right) \nabla \left(qT\right) = \nabla T_{\mathrm{dry}} + \nabla T_{\mathrm{moist}} \tag{2}$$

where T_{dry} involves is the T-only part and $\nabla T_{\mathrm{moist}} = \left(\frac{R_v}{Rd} - 1\right)\left(q\nabla T + T\nabla q\right)$ is the q and T part. A basic scale analysis, where $q = 10^{-2}$, $T = 10^2$ K, and horizontal gradients are represented by $\delta q = 10^{-3}$ and $\delta T = 1$ K implies that ∇T_{dry} is typically one order of magnitude larger than $\nabla T_{\mathrm{moist}}$. Futhermore, $T\nabla q$ is typically one order of magnitude larger than $q\nabla T$. This suggests that horizontal moisture gradients can only be significant contributor to the surface PGF when horizontal temperature gradients are relatively small (Yang, 2018a, 2018b).

2.4 Slab Boundary Layer Model Experiments

A zonally symmetric, slab boundary layer model (SBLM) on the sphere (Gonzalez & Schubert, 2019) is employed to simulate the boundary layer dynamics of the east Pacific Ocean forced by ERA5's boundary layer height, free tropospheric velocities (700–800 hPa averaged zonal and meridional velocity fields), and the estimated surface meridional PGF.

Consider zonally symmetric motions that depend on time t and latitude ϕ of an incompressible fluid of a frictional boundary layer of variable depth h. The boundary layer zonal and meridional velocities $u(\phi, t)$ and $v(\phi, t)$ are independent of height between the top of a thin surface layer and height, h, and the vertical velocity at the top of the boundary layer is denoted by $w(\phi, t)$. The governing system of differential equations is

$$\frac{\partial u}{\partial t} + v\frac{\partial u}{a\partial \phi} = f_e v - c_D U\frac{u}{h} + \frac{w^-}{h}\left(u - u_{\mathrm{FT}}\right) + K_u, \tag{3}$$

$$\frac{\partial v}{\partial t} + v\frac{\partial v}{a\partial \phi} = -f_e u - c_D U\frac{v}{h} - R_d T_v\frac{\partial \ln p}{a\partial \phi} + \frac{w^-}{h}\left(v - v_{\mathrm{FT}}\right) + K_v, \tag{4}$$

$$w = -\frac{\partial(hv\cos\phi)}{a\cos\phi\partial\phi}, \tag{5}$$

where $f_e = \left(2\Omega\sin\phi + \frac{u\tan\phi}{a}\right)$ is the effective Coriolis force, including the metric term, Ω and a are Earth's rotation rate and radius, $c_D U$ is the parameterized surface wind drag factor (more details below), $U = 0.78\left(u^2 + v^2\right)^{1/2}$ is the wind speed at 10 meter height (Powell et al., 2003), $w^- = \frac{1}{2}\left(|w| - w\right)$ is the rectified Ekman suction, $u_{\mathrm{FT}}(\phi)$ and $v_{\mathrm{FT}}(\phi)$ are the respective zonal and meridional velocities in the overlying free troposphere, $K_u = K\frac{\partial}{a\partial\phi}\left(\frac{\partial(hu\cos\phi)}{a\cos\phi\partial\phi}\right)$ is the zonal diffusion, $K_v = K\frac{\partial}{a\partial\phi}\left(\frac{\partial(hv\cos\phi)}{a\cos\phi\partial\phi}\right)$ is the meridional diffusion, and K is the constant horizontal diffusivity. The drag factor $c_D U$ is assumed to depend on the 10 meter wind speed according to the following formula from (Large et al., 1994)

$$c_D U = 10^{-3}\left(2.70 + 0.142U + 0.0764U^2\right). \tag{6}$$

A derivation of the SBLM equations starting from first conservation principles is given in the Appendix of Gonzalez and Schubert (2019). For all experiments, the constants used are $\Omega = 7.292 \times 10^{-5}$ s^{-1}, $a = 6.371 \times 10^6$ m, $K = 1.0 \times 10^6$ m^2 s^{-1}, $\Delta t = 300$ s, and $a * \Delta\phi = 0.25°$.

We perform a suite of SBLM simulations, one for each month of the year and over four different experiments for a total of 48 simulations (see Table 1). Each of the four SBLM experiments contains the same boundary layer height and free tropospheric velocity forcings but they have a different surface PGF forcing. The surface PGF forcings for each experiment are: i) surface PGF from surface to 850 hPa, mass-weighted and vertically-integrated T_v gradients (Full T_v), ii) surface PGF only from SST gradients (SST-only), iii) surface PGF only from T_v gradients averaged over 850–900 hPa ($T_{v,850-900}$), and iv) surface PGF only from 850 hPa PGF (PGF$_{850}$).

For all experiments, horizontal gradients are computed before selecting ocean-only points and before computing pressure level averages. Given that the Full T_v SBLM experiments involve numerical integration, we quantify the month-by-month errors in the Full T_v surface PGF against the "observed" surface PGF in Figure S1. The observed surface PGF is estimated using second-order central finite difference methods via the equation,

$$-\frac{1}{\rho_s}\nabla p_s = -R_d\left(\mathrm{SST}\right)\nabla\ln p_s, \tag{7}$$

where SST is the sea surface temperature. We find that the numerically integrated Full T_v surface PGF is quite accurate, with a minimum pattern correlation of 0.999 and a maximum standardized root-mean-squared difference of 0.066 compared to the estimate from equation (7). Note since the SBLM is a zonally symmetric model, only the meridional component ($\partial/\partial y$) of the surface PGF is used in this study. However, the use of the ∇ gradient operator is retained to keep the derivations as general as possible for future applications.

For the SST-only SBLM experiment, the assumption is that T_v gradients linearly decay with pressure (Lindzen & Nigam, 1987; Back & Bretherton, 2009a; Duffy et al., 2020) according to the formula

$$\nabla T_v(p) = \nabla\mathrm{SST}\left(1 - \delta_T\frac{(p_s - p)}{(p_s - p_T)}\right), \tag{8}$$

Table 1. The four SBLM experiments, including the numerical equations used to estimate the surface PGF forcings. We use $p_T = 850$ hPa for all experiments and $p_s = 1013$ hPa for only the SST and $T_{v,850-900}$ experiments. For Full T_v, the SST is used in place of T_v at the surface and the surface pressure is the observed mean sea level pressure, i corresponds to each pressure level from the surface to 850 hPa, and N is the total number of pressure levels. In the $T_{v,850-900}$ experiment, the overbar represents an average over 850–900 hPa.

Experiment	Surface PGF Equation
Full T_v	$R_d \sum_{i=1}^{N-1} (\nabla T_{v_i}) \ln\left(\frac{p_{i+1}}{p_i}\right) - (\nabla\Phi)_{p_T}$
SST-only	$R_d A\,(\nabla \text{SST}) \ln\left(\frac{p_s}{p_T}\right) - (\nabla\Phi)_{p_T}$
$T_{v,850-900}$	$R_d \left(\overline{\nabla T_v}\right) \ln\left(\frac{p_s}{p_T}\right) - (\nabla\Phi)_{p_T}$
PGF_{850}	$-(\nabla\Phi)_{p_T}$

where δ_T is a fraction representing how fast the SST gradient linearly decays from the surface, p_s, to the top of the boundary layer, p_T. For this study, we choose $\delta_T = 0.75$, which implies that the SST gradients have decayed by 75% at $p = p_T$. The assumption of the SST gradient only changing in magnitude in the vertical allows for the surface PGF forcing formula in (1) to be written as

$$-(\nabla\Phi)_{p_s} = R_d \ln\left(\frac{p_s}{p}\right) A\nabla\text{SST} - (\nabla\Phi)_p\,, \tag{9}$$

where

$$A = 1 - \delta_T \left(\frac{p_s}{p_s - p_T} - \frac{1}{\ln(p_s/p_T)}\right). \tag{10}$$

Using the constant values $p_s = 1013$ hPa, $p_T = 850$ hPa, and $\delta_T = 0.75$, $A = 0.614$, which implies that the net amplitude (when verticall integrated) of the SST gradient on the surface PGF is 61.4% due to the assumption of the SST gradient decaying linearly with height.

For the $T_{v,850-900}$ experiment, we assume that T_v gradients at 850–900 hPa are the same in amplitude and pattern throughout the entire boundary layer, which allows for the surface PGF forcing formula in (1) to be written as

$$-(\nabla\Phi)_{p_s} = R_d \ln\left(\frac{p_s}{p}\right) \overline{\nabla T_v} - (\nabla\Phi)_p\,, \tag{11}$$

where the overbar represents a pressure level average after the computation of T_v gradients (only the meridional component in this study). See Table 1 for the exact form of the surface PGF equation for each of the SBLM experiments.

Note that for the entirety of the paper, SBLM simulation solutions will be shown at the equilibrium time of 30 days, which is when the meridional integral of the kinetic energy and its tendency vanish over the entire domain (not shown). For comparisons between the dynamical solutions of the SBLM versus boundary layer (850–1000 hPa) averaged ERA5 data, see Figures S2 and S3 in the Supporting Information section.

3 Results

3.1 ERA5 Surface PGF SBLM Forcings

To help with our interpretations of the SBLM surface PGF forcing fields for each of our four SBLM experiements, Figure 1a,b shows the "surface geopotential anomaly" during the contrasting months of September and March using ERA5 data. The surface geopotential anomaly is technically the latitudinally integrated surface PGF field from Figure 1c,d with the 15°S–15°N mean removed. Since all four experiments have the same 850 hPa PGF, panels e and f show the surface PGF that comes solely from T_v gradients. We examine the surface PGF (and its surface geopotential anomaly) because it is our only varying forcing between our four SBLM experiments and it is one of the three leading terms in the meridional momentum budget in all of our SBLM simulations, as shown in Figure S4.

The surface geopotential anomalies associated with all four surface PGF forcings show broadly that September is dominated by high geopotential south of the equator and low geopotential north of the equator (Figure 1a). From this general latitudinal structure of geopotential, one would expect a northern ITCZ to develop in all SBLM simulations. During March, all four surface PGF forcings also show qualitative agreement that surface geopotential anomalies are nearly symmetric about the equator with low geopotential anomalies centered on the equator (Figure 1b). Thus, one would expect either one single ITCZ centered on the equator or two ITCZs stradding the equator, a double ITCZ, during March. A double ITCZ structure typically occurs when there is a relatively high geopotential centered on the equator (Figure 1b) or the surface PGF switches from negative to positive abruptly near the equator (Figure 1d,f,), inducing divergence away from the equator (Gonzalez et al., 2016). Thus, we anticipate a double ITCZ to be produced from the SST-only and Full T_v (to a lesser extent) SBLM simulations during March (Figure 1b,d,f, blue curves). Despite many broad similarities between all four surface PGF forcings, there are key differences between the SBLM surface PGF forcings for Full T_v (black), SST-only (blue), and $T_{v,850-900}$ (red).

South of the equator during both September and March, the high surface geopotential anomalies and PGF are consistently weaker in SST-only (Figure 1a–d, blue curves) than in Full T_v (black curves) and $T_{v,850-900}$ (red curves). This would suggest that SST-only SBLM simulations have an anomalous low south of the equator and too much southern hemisphere convergence. Near the equator during September and March, SST-only surface geopotential anomalies are anomalously higher than Full T_v and $T_{v,850-900}$ (Figure 1a,b), implying there may be excessive equatorial divergence in SST-only SBLM simulations. North of the equator, comparisons of surface geopotential anomalies and surface PGF between SST-only versus Full T_v and $T_{v,850-900}$ are a bit messier than they are near and south of the equator. However, SST-only surface geopotential anomalies are anomalously higher than in T_v and $T_{v,850-900}$ north of 4°N during September and from 4°N–8°N during March. Given that the ITCZ is located near 5°N–15°N in September and 3–8°N in March (Liu & Xie, 2002), one would expect these anomalously high surface geopotential anomalies to yield weaker ITCZ convergence in SST-only than in Full T_v or $T_{v,850-900}$ SBLM simulations.

3.2 Boundary Layer Wind Convergence from the Four SBLM Experiments

Figure 2c,d illustrates that SST-only SBLM simulations produce a year-round double ITCZ and excessive equatorial divergence compared to Full T_v SBLM simulations. In observations and reanalyses, a double ITCZ peaks during February through April (C. Zhang, 2001; Liu & Xie, 2002; Gu et al., 2005; Gonzalez et al., 2022). Similar to the Full T_v SBLM simulations in Figure 2a, the $T_{v,850-900}$ SBLM simulations (Figure 2e) also prefer a northern hemisphere ITCZ. However, near-equatorial divergence is shifted northward (up to

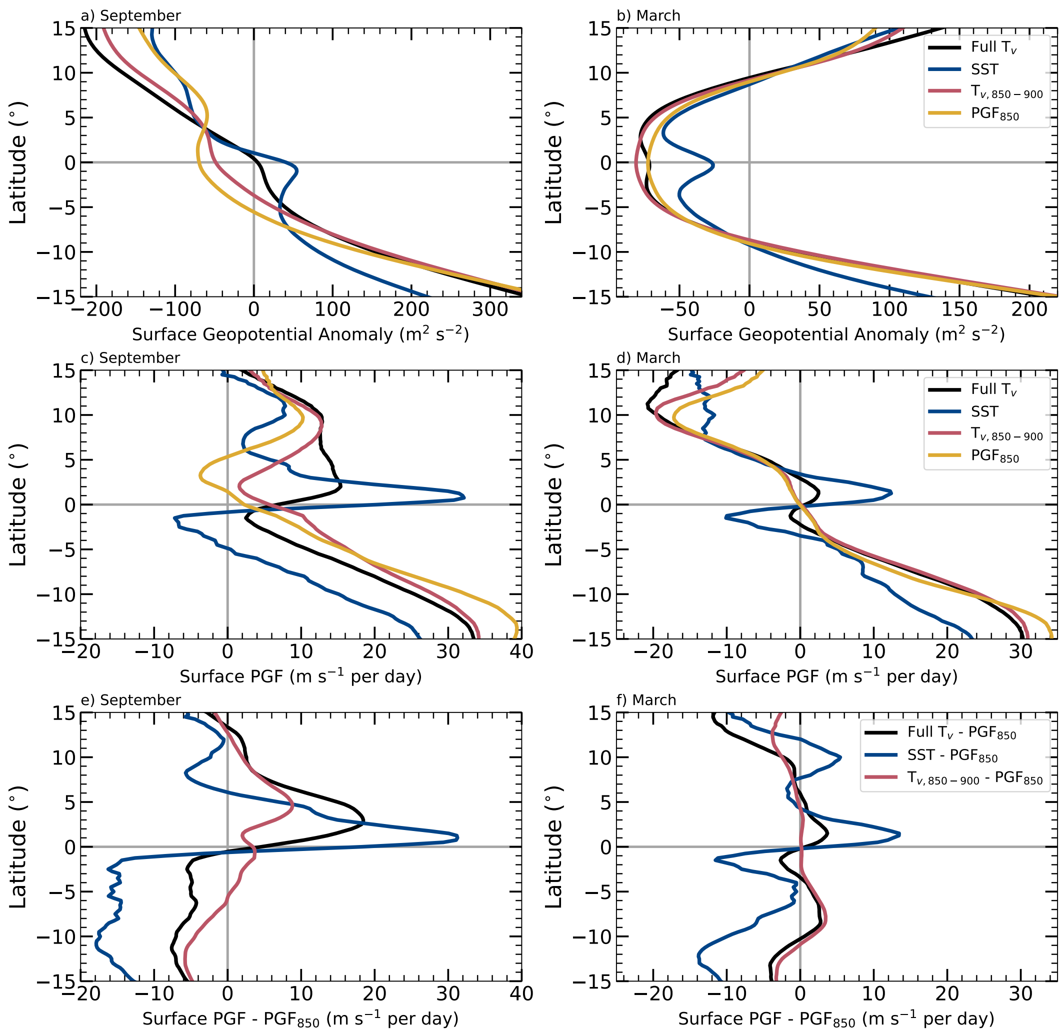

Figure 1. ERA5 surface geopotential anomaly and pressure gradient force (PGF) averaged over the east Pacific Ocean (90–125°W) for the four SBLM experiments (see Table 1): Full T_v (black), SST-only (blue), $T_{v,850-900}$ (red), and PGF_{850} (gold) during the months of a,c,e) September and b,d,f) March. ERA5 surface geopotential anomaly (relative to the 15°S–15°N mean) during a) September and b) March. ERA5 surface PGF during c) September and d) March. ERA5 surface PGF minus PGF_{850} during e) September and f) March.

4°N) and is only present from June through October. Equatorial convergence is present year-round in both the $T_{v,850-900}$ and PGF_{850} simulations (Figure 2b). PGF_{850} simulations contain off-equatorial divergence and equatorial convergence that is nearly symmetric about the equator during May through December, in large contrast to the Full T_v and $T_{v,850-900}$ simulations. These quasi-symmetric features of the PGF_{850} boundary layer convergence during May through December highlight the importance of north-south asymmetries in boundary layer T_v in the production a northern hemisphere-dominant ITCZ in observations.

From Figure 2d, it is evident that SST-only SBLM simulations overproduce equatorial divergence and southern hemisphere convergence. However, how significant the convergence pattern biases are in SST-only SBLM simulations relative to Full T_v SBLM sim-

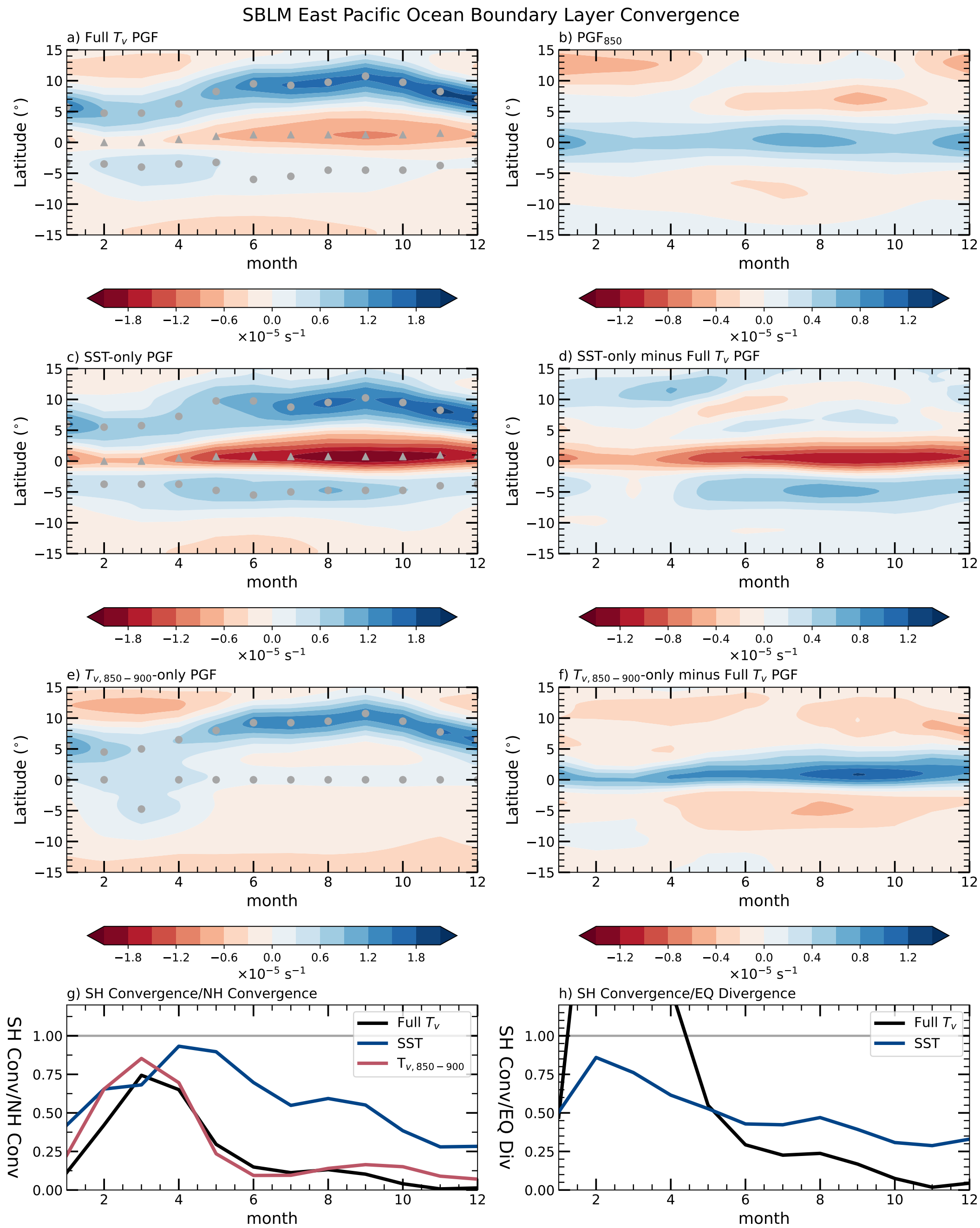

Figure 2. SBLM-simulated boundary layer convergence over the east Pacific Ocean (90-125°W) for the four experiments: a) Full T_v PGF, b) PGF_{850}, c) SST-only PGF, and e) $T_{v,850-900}$-only PGF. Panel d shows SST-only minus Full T_v PGF and panel f shows $T_{v,850-900}$-only minus Full T_v PGF. Panel g shows the ratio of the maxima of NH convergence and SH convergence and panel h shows the ratio of the maxima of equatorial divergence and SH convergence for the Full T_v PGF (black), SST-only PGF (blue), and $T_{v,850-900}$-only PGF (red). In panels a, c, and e, the gray circles are the latitudes of maximum SH and NH convergence and the gray triangles are the latitudes of maximum equatorial divergence.

ulations is not as clear. This is relevant since SH convergence is present all year in the Full T_v SBLM simulations and in observations (Liu & Xie, 2002; Gonzalez et al., 2022) but it is relatively weak for most of the year, especially compared to northern hemisphere (NH) convergence. Panels g of Figure 2 suggest there is indeed a substantial pattern problem in SST-only SBLM simulations in that SH convergence is two to five times too strong compared to NH convergence for all months except from February through April. Furthermore, SST-only SBLM simulations have excessive SH convergence compared to equatorial (EQ) divergence (one and a half to five times too strong) during June through December (Figure 2h). February through April also shows substantial discrepancies in SST-only SBLM simulations, with EQ divergence being three to four times too strong compared to SH convergence (Figure 2h). Meanwhile, the $T_{v,850-900}$ SH/NH convergence ratio is also an accurate predictor of the latitudinal asymmetry in ITCZ convergence (Figure 2g, red curves). However, caution is taken with our interpretation of the $T_{v,850-900}$ SBLM simulations as there is not well-defined divergence or convergence near the equator (why $T_{v,850-900}$ is not shown in Figure 2h). Overall, we center the rest of our analyses on the idea that SH convergence is too strong compared to EQ divergence and NH convergence in SST-only SBLM simulations during the months of June through December, peaking in September.

3.3 Connection to the Variation of Virtual Temperature Gradients within the Boundary Layer

To better visualize the contrasting roles of upper boundary layer and near surface meridional T_v gradients on ITCZ convergence, we compare the vertical structure of SST gradient-driven T_v gradients using equation (8) with those using observed T_v gradients.

Figure 3a,b shows that both observed and SST gradient-driven T_v gradients broadly agree that there are northward T_v gradients everywhere except from 5–10°S to the equator which is where the equatorial cold tongue exists. Figure 3c shows that most of the differences occur in the upper boundary layer, as expected, but the largest differences are present throughout the boundary layer near the equator. There is a strong southward T_v gradient anomaly because the equatorial cold tongue signal is weaker in the observed T_v gradient than the SST gradient-driven T_v gradient and it is also shifted slightly north. Upper boundary layer T_v gradient anomalies highlight that there are consistently stronger northward T_v gradients above the surface. In other words, there is a significant change in the T_v gradient with height within the boundary layer. For example, there is a complete reversal in the T_v gradient with height over 6°S–EQ, which we hypothesize plays a role in mitigating the southern hemisphere ITCZ in SST-only SBLM simulations. In addition, there is a northward tilt in the northward T_v gradient with height near 5°N that is not present in SST gradient-driven T_v gradients. Figure 3d,e show that most of the differences in observed and SST gradient-driven T_v gradients are due to temperature gradient ($\partial T_{\mathrm{dry}}/\partial y$) differences with moisture gradient effects ($\partial T_{\mathrm{moist}}/\partial y$) being of secondary importance. Moisture gradient effects act to increase northward temperature gradients, especially south of the ITCZ and in the upper boundary layer where moisture gradients are largest.

Figure 4a,b shows that observed and SST gradient-driven T_v gradients are generally weaker during March than September. Differences between these T_v gradients are largest in the upper boundary layer south of 5°S but they are otherwise quite weak (Figure 4c). Similar to September, the cold tongue signature is weaker and shallower in the observed T_v gradient compared to the SST gradient-driven T_v gradient. Furthermore, the southward T_v gradient just south of the equator reverses to northward T_v gradient near 925 hPa, albeit it is quite weak compared to September. Figure 4d,e also show that most of the differences in observed and SST gradient-driven T_v gradients are due to temperature gradient ($\partial T_{\mathrm{dry}}/\partial y$) differences, however, moisture gradient effects ($\partial T_{\mathrm{moist}}/\partial y$) do play a relatively larger role in March compared to September. This is not surprising based on our crude scale analysis in section 2.3, as we expected moisture gradient effects to be most significant during months when temperature gradients are smallest. Another interesting feature in this decomposition is that moisture gradient effects do not strictly enhance temperature gradients. For example, moisture gradients work against temperature gradients as it is anomalously warm and dry near the equator in the observed T_v gradient compared to the SST gradient-driven T_v gradient.

Since it may be difficult to conceptualize T_v gradients, Figure 5 shows the vertical structure of the observed T_v, SST gradient-driven T_v, and T_v - SST gradient-driven T_v for September and March. The observed and SST gradient-driven T_v anomalies for September show the broad northward T_v gradient over the domain with an equatorial cold tongue. However, the observed T_v anomaly shows a cold anomaly 15–20 degrees south of the equatorial cold tongue that twice as strong and is situated well above the surface. At the same time, the equatorial cold tongue signature is weaker in the observed T_v anomaly compared to the SST gradient-driven T_v anomaly. It is this cold anomaly that aids in weakening the southern hemisphere convergence and it is the weaker cold tongue that subdues the equatorial divergence seen in the SST-only SBLM simulations during September (and more generally, June through December). Furthermore, there is a warm anomaly above the surface near 15°N that helps explain the slight underestimation of northern hemisphere convergence in SST-only SBLM simulations (Figure 2a–b).

The observed and SST gradient-driven T_v anomalies for March show broad similarities with relatively warm air north of the equator and a cold anomaly south of 8–9°S. However, SST gradient-driven T_v anomalies show an equatorial cold tongue signature that is absent from the observed T_v anomalies. This feature helps explain why the main bias in the SST-only SBLM simulations during March (and more generally, February–April) is excessive equatorial divergence (Figure 2a–b). Fortunately, the discrepancies in SST gradient-driven T_v anomalies suring March do not have a significant effect on the double ITCZ compared to September.

3.4 Connection to the TWI and Low Clouds

To better quantify the reasons for the seasonal change in the equatorial and southern hemisphere meridional T_v gradients within the context of the TWI, Figure 6a,b shows the disappearance of the TWI from September to March in ERA5. Associated with the TWI during September is a clear difference in vertical structure of T_v at both 7.5°S and the EQ compared to the 30°S–30°N domain (Figure 6c) such that both locations experience relative warming above cooling, with the cool anomaly at 7.5°S centered well above the surface at 900 hPa and the maximum cooling at/near the surface at the EQ. To come back to the connection between the TWI and changing meridional T_v gradients with height, Figure 6d computes the difference between the September 7.5°S and EQ T_v profiles. The differences in vertical T_v structure between 7.5°S and the EQ suggest there is an increased north-south T_v gradient in the upper part of the boundary layer (cooler to the south) and a decreased temperature gradient near the surface (cooler at the EQ). It is the displacement of these two cool anomalies that causes the differences in the resulting surface PGF and boundary layer convergence between Full T_v and SST-only SBLM simulations (Figures 1 and 2).

Near the surface, the SST cold tongue signature at the equator causes a high surface pressure and a prominent double ITCZ structure while in the upper boundary layer, the cool anomaly is displaced south of the equator which contributes to a displacement of the high surface pressure south of the equator and a relaxation of the double ITCZ structure. These effects are due to the localized (at the equator and in the SH) changes in lapse rates in the 800–900 hPa layer, which are tied to the presence of the TWI and low-level cloud decks (namely, stratocumulus clouds). How do we suspect these features,

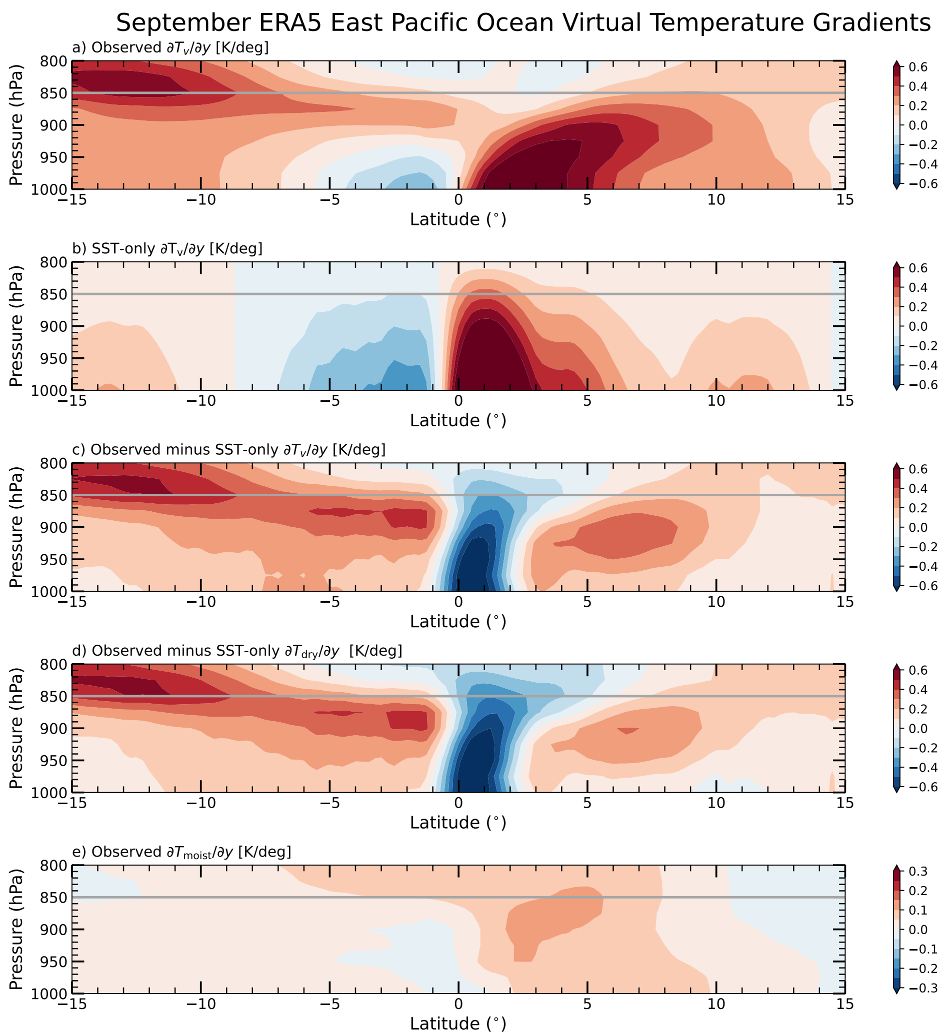

Figure 3. Meridional T_v gradients averaged over the east Pacific Ocean (90-125°W) during September: a) observed $\partial T_v/\partial y$, b) SST-only $\partial T_v/\partial y$, c) observed minus SST-only $\partial T_v/\partial y$, d) observed minus SST-only $\partial T_{\mathrm{dry}}/\partial y$, and e) observed $\partial T_{\mathrm{moist}}/\partial y$.

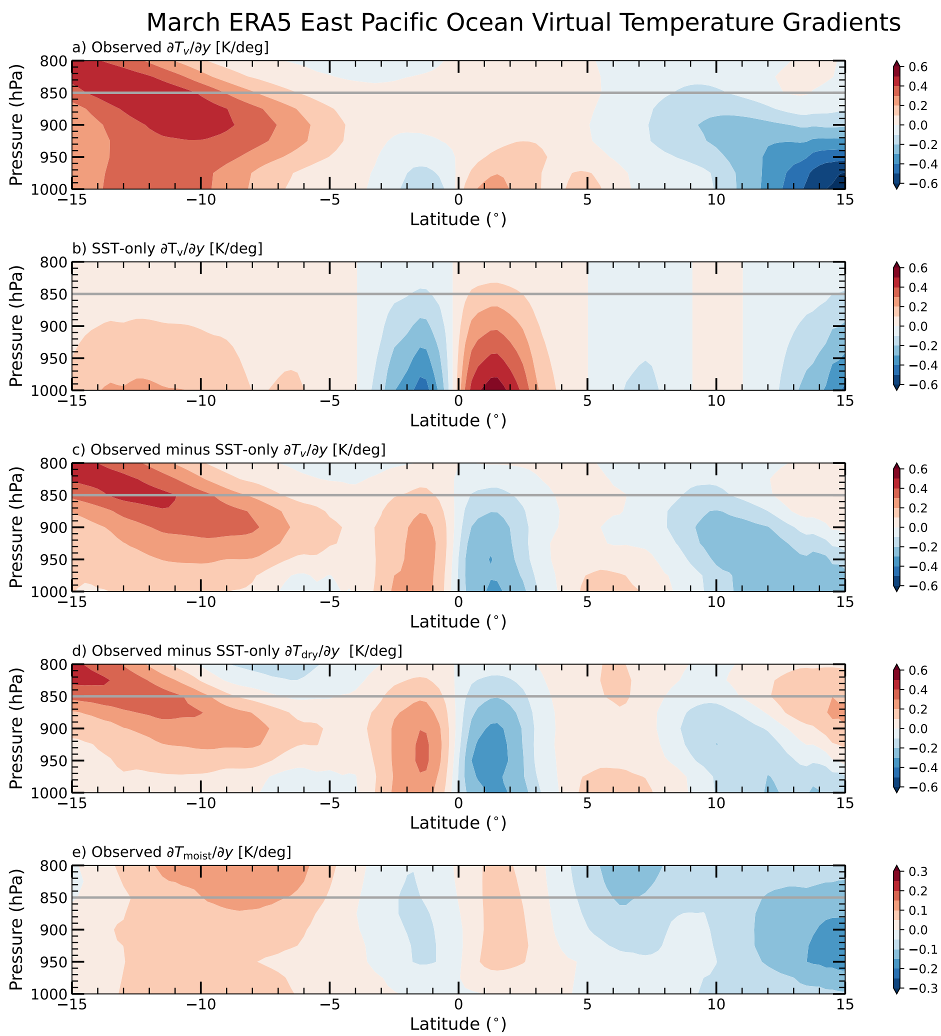

Figure 4. Same as Figure 3 but for March.

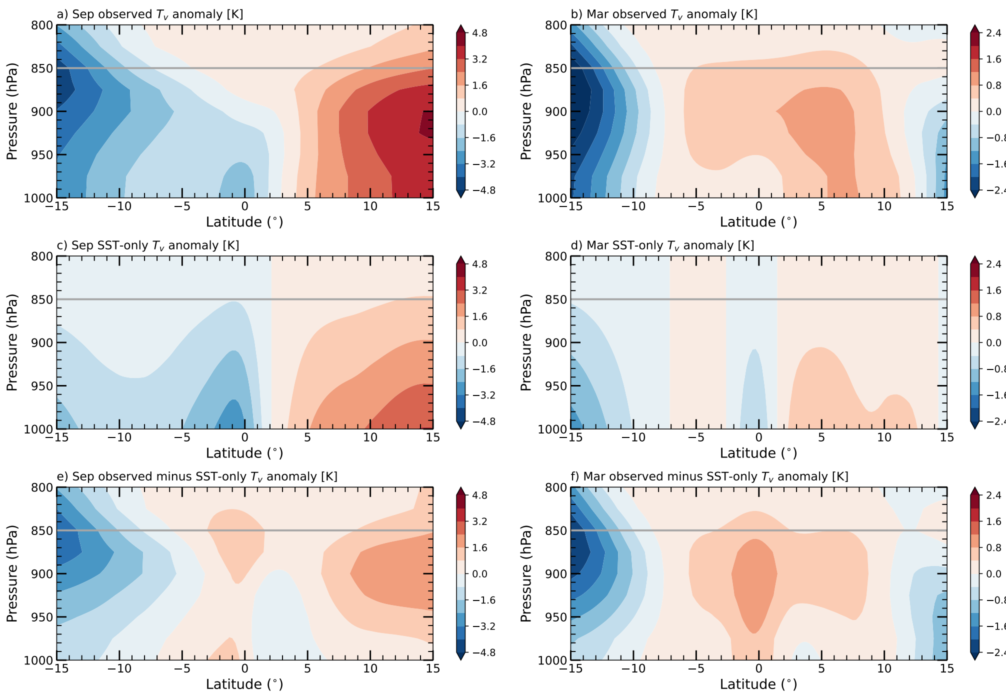

Figure 5. T_v anomaly averaged over the east Pacific Ocean (90-125°W) during September (left) and March (right): a,b) observed T_v, c,d) SST-only T_v, and e,f) observed minus SST-only T_v. Anomalies are relative to the 15°S–15°N average.

e.g., TWI stronger to the south, are related to stratocumulus clouds? The next section provides evidence to support these arguments.

Figure 7 show the stratocumulus (Sc) cloud fraction in a) GOCCP CASCCAD and b) CloudSat-CALIPSO at 7.5°S (shaded) and EQ (black contour lines) as a function of month of the year and averaged over the east Pacific (90-125°W). As expected, the Sc cloud fraction maximizes just below the 850 hPa level (1.2 km) during August through October in a similar way as TWI layer lapse rates minimize during September in ERA5. Sc cloud fraction minimizes during February through April, which also agrees with the maxima in TWI layer lapse rates during March in ERA5. Despite slightly different magnitude of Sc cloud fraction between the Cloudsat-CALIPSO CASCCAD and GOCCP CASCCAD, the two datasets show general seasonal agreement, especially at 7.5°S. One noticeable difference is that Cloudsat-CALIPSO CASCCAD shows a peak in Sc cloud fraction at the EQ that is slightly lower in altitude (700 m–1 km) compared to GOCCP CASCCAD (≈1.2 km). This shallower Sc feature is reminiscent of the equatorial TWI being located lower in height (875–900 hPa) than the 7.5°S TWI (850 hPa) in Figure 6a,b. A latitudinal cross-section during September supports the presence of this tilt of Sc low clouds with latitude, as shown in Figure S5. Despite a slightly smaller Sc % and a slight deviation in the height of maximum Sc %, GOCCP CASCCAD manages to capture Sc cloud fractions to the same extent as CloudSat-CALIPSO. This is even true during March when convection could attenuate the low cloud signal based on subsequent analyses of the vertical profiles of specific humidity and vertical pressure velocity (not shown).

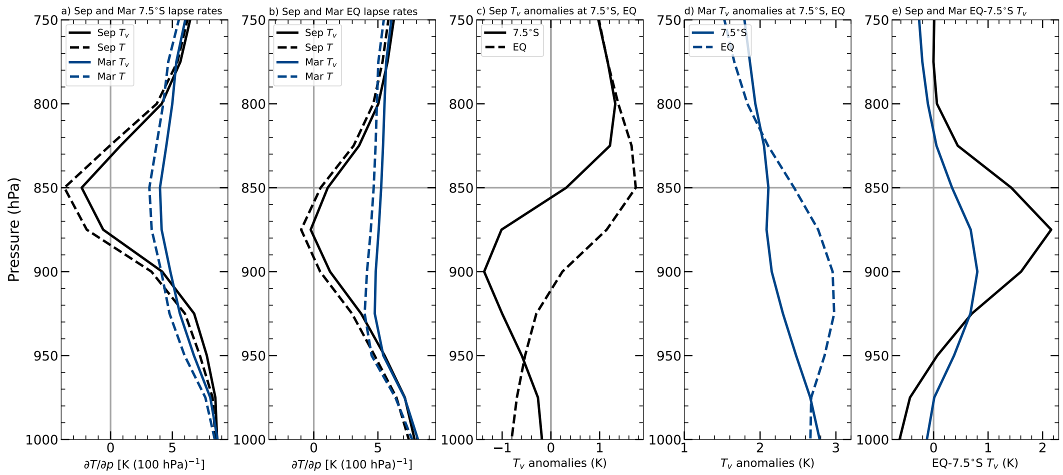

Figure 6. ERA5 $\partial T_v/\partial p$ (solid) and $\partial T/\partial p$ (dashed) over the east Pacific Ocean (90-125°W) at a) 7.5°S and b) EQ for September (black) and March (blue). T_v anomaly (relative to the 30°S–30°N annual mean T_v) at 7.5°S (solid) and EQ (dashed) for c) September (black) and d) March (blue). e) EQ minus 7.5°S T_v for September (black) and March (blue), which highlights the change in direction of the T_v gradient near 950–975 hPa.

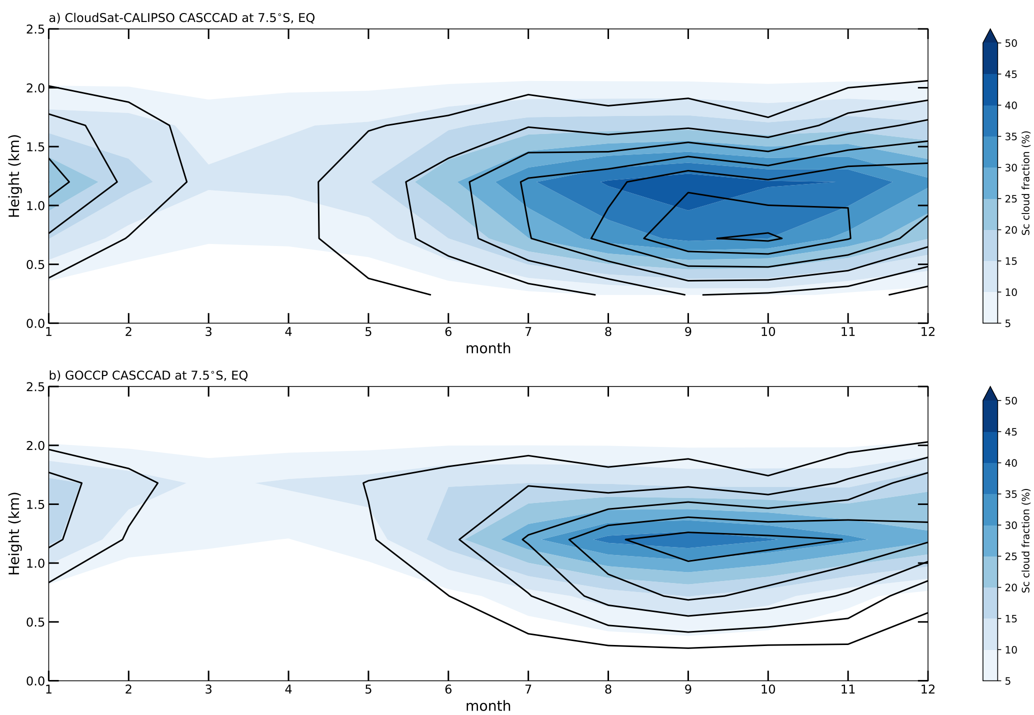

Figure 7. Stratocumulus (Sc) cloud fraction (%) averaged over the east Pacific Ocean (90-125°W) at 7.5°S (shaded) and EQ (black contour lines) as a function month and height for a) Cloudsat-CALIPSO CASCCAD (2007–2010) and b) GOCCP CASCCAD (2007–2016).

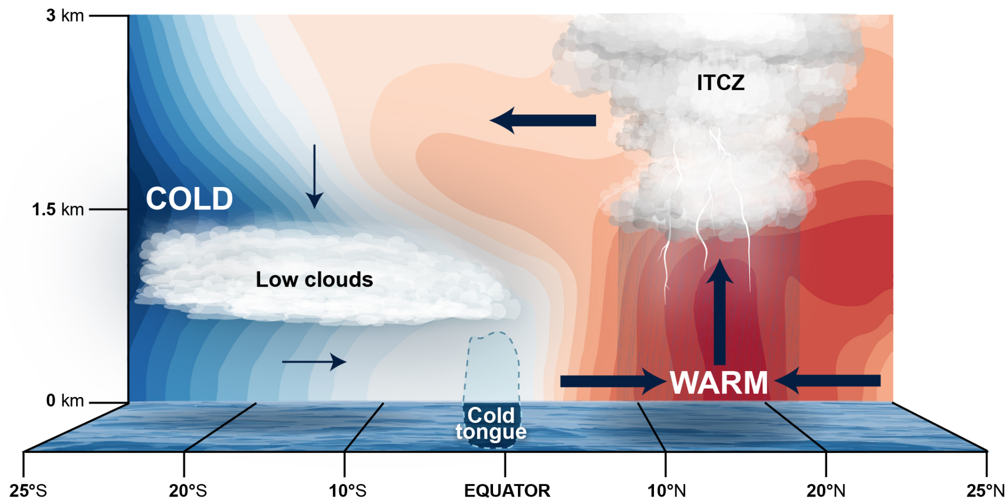

Figure 8. Conceptual figure of the importance of the cooling: i) at the top of Sc low clouds and ii) near the equatorial cold tongue on ITCZ wind convergence. (Contours) The ERA5 T_v anomaly (relative to the 30°S–30°N annual mean T_v) averaged over the east Pacific Ocean (90-125°W) during September.

4 Summary and Conclusions

In this study, we have illustrated the important role of meridional virtual temperature (T_v) gradients varying with height in the boundary layer on ITCZ wind convergence over the east Pacific Ocean on monthly timescales. We employed an idealized, slab boundary layer model to conduct four main experiments using different surface pressure gradient force (PGF) forcings from ERA5 reanalysis data: i) mass-weighted, boundary layer (surface–850 hPa) integrated T_v PGF (Full T_v), ii) SST-only PGF, iii) upper boundary layer (850–900 hPa) averaged T_v PGF ($T_{v,850-900}$), and iii) PGF at 850 hPa (PGF_{850}).

We find that two factors distinguish near-surface meridional T_v gradients from those in the upper boundary layer. Near the surface, there is an equatorial cold tongue that promotes strong equatorial divergence and off-equatorial divergence, a double ITCZ-like structure. In the upper boundary layer, there is a cool anomaly that is shifted 15 to 20 degrees south of the equator that is associated with a strong trade wind inversion (TWI) above it and a high amount of stratocumulus low clouds slightly below it. Presumably, this cool anomaly is associated with the longwave radiative cooling at the top of stratocumulus clouds and there is adiabtic warming above them (Figure 6c). Another interpretation (based on hydrostatic balance as a relationship between surface pressure and density of the atmosphere above) is that the ITCZ is less prevalent near the equator and south of the equator because the atmospheric column (mainly the boundary layer) is denser (cooler and drier) than it is north of the equator due to these two mechanisms. These mechanisms are not mutually exclusive, however, the TWI and low clouds typically have a relatively larger impact south of the equator while the cold tongue has a relatively larger impact near the equator. These main ideas are conceptualized in Figure 8.

Our SBLM experiments show that the largest discrepancies in ITCZ wind convergence between the SST-only and Full T_v SBLM simulations occur at the same time that the equatorial cold tongue, the TWI, and stratocumulus clouds peak in intensity during June through December. Our interpretation is that the upper boundary layer TWI and stratocumulus clouds help in providing a large-scale north to south (NH versus SH) asymmetry in ITCZ convergence as they mitigate the excessively strong equatorial divergence and SH ITCZ convergence that would otherwise be produced by the SST distribution alone.

While SST gradients can help explain essential features of the east Pacific ITCZ, such as the year-round weak convergence in the SH (Liu & Xie, 2002) and more latitudinally concentrated ITCZ convection (Gonzalez et al., 2016), T_v gradients well above the surface (but in the boundary layer) altered by low clouds also play a key role in the observed preference of a NH-dominant ITCZ in the east Pacific Ocean (Philander et al., 1996). We describe our findings within the framework of a "dynamical" link between the TWI/low clouds, the equatorial cold tongue, and the ITCZ mainly because we are defining ITCZ based on boundary layer wind convergence. However, there is much more to be learned about these connections and how other thermodynamics factors, such as low- to mid-free tropospheric moisture, moist static energy, and turbulent mixing fit into the big picture of what controls tropical convection in and near the ITCZ (Bony et al., 2017; Stevens et al., 2017; Fuchs-Stone et al., 2020; Raymond & Fuchs-Stone, 2021).

Open Research Section

The ERA5 reanalysis data on pressure levels can be downloaded from the URL: https://cds.climate.copernicus.eu/cdsapp#!/dataset/reanalysis-era5-pressure-levels. The CASCCAD data can be downloaded from: https://data.giss.nasa.gov/clouds/casccad/. All output from each of the four SBLM experiments can be downloaded from the URL: https://drive.google.com/drive/folders/1Ui8hqGZhq8VUbz7xrQ0LgxW8IT3MRVY-?usp=sharing.

Acknowledgments

We would like to acknowledge stimulating conversations with Kristopher Karnauskas and Richard Neale throughout the course of this project. Financial support comes from NSF Grant AGS-1953944.

References

Adam, O., Schneider, T., & Brient, F. (2018). Regional and seasonal variations of the double-ITCZ bias in CMIP5 models. *Climate Dyn.*, *51*, 101–117. doi: 10.1007/s00382-017-3909-1

Back, L. E., & Bretherton, C. S. (2009a). On the relationship between SST gradients, boundary layer winds and convergence over the tropical oceans. *J. Climate*, *22*, 4182–4196. doi: 10.1175/2009JCLI2392.1

Back, L. E., & Bretherton, C. S. (2009b). A simple model of climatological rainfall and vertical motion patterns over the tropical oceans. *J. Climate*, *22*(23), 6477–6497. Retrieved from `https://doi.org/10.1175/2009JCLI2393.1` doi: 10.1175/2009JCLI2393.1

Bony, S., Stevens, B., Ament, F., Bigorre, S., Chazette, P., Crewell, S., ... Wirth, M. (2017). EUREC4A: A Field Campaign to Elucidate the Couplings Between Clouds, Convection and Circulation. *Surveys in Geophysics*, *38*, 1529–1568. Retrieved from `https://doi.org/10.1007/s10712-017-9428-0` doi: 10.1007/s10712-017-9428-0

Bretherton, C. S., Uttal, T., Fairall, C. W., Yuter, S. E., Weller, R. A., Baumgardner, D., ... Raga, G. B. (2004). The epic 2001 stratocumulus study. *Bulletin of the American Meteorological Society*, *85*(7), 967 - 978. Retrieved from `https://journals.ametsoc.org/view/journals/bams/85/7/bams-85-7-967.xml` doi: 10.1175/BAMS-85-7-967

Cesana, G., Del Genio, A. D., & Chepfer, H. (2019). The cumulus and stratocumulus cloudsat-calipso dataset (casccad). *Earth System Science Data*, *11*(4), 1745–1764. Retrieved from `https://essd.copernicus.org/articles/11/1745/2019/` doi: 10.5194/essd-11-1745-2019

Cesana, G., & Waliser, D. E. (2016). Characterizing and understanding systematic biases in the vertical structure of clouds in cmip5/cfmip2 models. *Geophysical Research Letters*, *43*(19), 10,538-10,546. Retrieved from `https://agupubs.onlinelibrary.wiley.com/doi/abs/10.1002/2016GL070515` doi: https://doi.org/10.1002/2016GL070515

Chelton, D. B., Esbensen, S. K., Schlax, M. G., Thum, N., Freilich, M. H., Wentz, F. J., … Schopf, P. S. (2001). Observations of coupling between surface wind stress and sea surface temperature in the eastern tropical pacific. *Journal of Climate*, *14*(7), 1479 - 1498. Retrieved from `https://journals.ametsoc.org/view/journals/clim/14/7/1520-0442_2001_014_1479_oocbsw_2.0.co_2.xml` doi: 10.1175/1520-0442(2001)014⟨1479:OOCBSW⟩2.0.CO;2

Chepfer, H., Bony, S., Winker, D., Cesana, G., Dufresne, J. L., Minnis, P., … Zeng, S. (2010). The gcm-oriented calipso cloud product (calipso-goccp). *Journal of Geophysical Research: Atmospheres*, *115*(D4). Retrieved from `https://agupubs.onlinelibrary.wiley.com/doi/abs/10.1029/2009JD012251` doi: https://doi.org/10.1029/2009JD012251

Duffy, M. L., O'Gorman, P. A., & Back, L. E. (2020). Importance of laplacian of low-level warming for the response of precipitation to climate change over tropical oceans. *Journal of Climate*, *33*(10), 4403 - 4417. Retrieved from `https://journals.ametsoc.org/view/journals/clim/33/10/jcli-d-19-0365.1.xml` doi: 10.1175/JCLI-D-19-0365.1

Fuchs-Stone, v., Raymond, D. J., & Sentić, S. (2020). Otrec2019: Convection over the east pacific and southwest caribbean. *Geophysical Research Letters*, *47*(11), e2020GL087564. Retrieved from `https://agupubs.onlinelibrary.wiley.com/doi/abs/10.1029/2020GL087564` (e2020GL087564 2020GL087564) doi: https://doi.org/10.1029/2020GL087564

Gonzalez, A. O., Ganguly, I., McGraw, M. C., & Larson, J. G. (2022). Rapid dynamical evolution of itcz events over the east pacific. *Journal of Climate*, *35*(4), 1197 - 1213. Retrieved from `https://journals.ametsoc.org/view/journals/clim/35/4/JCLI-D-21-0216.1.xml` doi: 10.1175/JCLI-D-21-0216.1

Gonzalez, A. O., & Schubert, W. H. (2019). Violation of Ekman balance in the eastern Pacific ITCZ boundary layer. *J. Atmos. Sci.*, *76*(9), 2919–2940. doi: 10.1175/JAS-D-18-0291.1

Gonzalez, A. O., Slocum, C. J., Taft, R. K., & Schubert, W. H. (2016). Dynamics of the ITCZ boundary layer. *J. Atmos. Sci.*, *73*(4), 1577–1592. doi: 10.1175/JAS-D-15-0298.1

Gu, G., Adler, R. F., & Sobel, A. H. (2005). The eastern Pacific ITCZ during the boreal spring. *J. Atmos. Sci.*, *62*, 1157–1174.

Haman, K. E., Malinowski, S. P., Kurowski, M. J., Gerber, H., & Brenguier, J.-L. (2007). Small scale mixing processes at the top of a marine stratocumulus—a case study. *Quarterly Journal of the Royal Meteorological Society*, *133*(622), 213-226. Retrieved from `https://rmets.onlinelibrary.wiley.com/doi/abs/10.1002/qj.5` doi: https://doi.org/10.1002/qj.5

Hayes, S. P., McPhaden, M. J., & Wallace, J. M. (1989). The influence of sea surface temperature on surface wind in the eastern equatorial Pacific: Weekly to monthly variability. *J. Climate*, *2*, 1500–1506.

Hersbach, H., & coauthors. (2020). The ERA5 global reanalysis. *Quart. J. Roy. Meteor. Soc.*, *146*(730), 1999–2049. doi: 10.1002/qj.3803

Holton, J. R. (1975). On the influence of boundary layer friction on mixed Rossby-gravity waves. *Tellus*, *27*, 107–115. doi: 10.1111/j.2153-3490.1975.tb01664.x

Holton, J. R., Wallace, J. M., & Young, J. A. (1971). On boundary layer dynamics and the ITCZ. *J. Atmos. Sci.*, *28*, 275–280. doi: 10.1175/1520-0469(1971)028⟨0275:OBLDAT⟩2.0.CO;2

Karnauskas, K. B. (2022). A simple coupled model of the wind–evaporation–sst feedback with a role for stability. *Journal of Climate*, *35*(7), 2149 - 2160. Retrieved from `https://journals.ametsoc.org/view/journals/clim/35/7/JCLI-D-20-0895.1.xml` doi: 10.1175/JCLI-D-20-0895.1

Klein, S. A., & Hartmann, D. L. (1993). The seasonal cycle of low stratiform clouds. *Journal of Climate*, *6*(8), 1587 - 1606. Retrieved from `https://journals.ametsoc.org/view/journals/clim/6/8/1520-0442_1993_006_1587_tscols_2_0_co_2.xml` doi: 10.1175/1520-0442(1993)006⟨1587:TSCOLS⟩2.0.CO;2

Large, W. G., McWilliams, J. C., & Doney, S. C. (1994). Oceanic vertical mixing: A review and a model with a nonlocal boundary layer parameterization. *Rev. Geophys.*, *32(4)*, 363–403. doi: 10.1029/94RG01872

Li, G., & Xie, S.-P. (2014). Tropical Biases in CMIP5 Multimodel Ensemble: The Excessive Equatorial Pacific Cold Tongue and Double ITCZ Problems. *J. Climate*, *27*(4), 1765–1780. doi: 10.1175/JCLI-D-13-00337.1

Lin, J.-L. (2007). The double-ITCZ problem in IPCC AR4 coupled GCMs: Ocean–atmosphere feedback analysis. *J. Climate*, *20*(18), 4497-4525. doi: 10.1175/JCLI4272.1

Lindzen, R. S., & Nigam, S. (1987). On the role of sea surface temperature gradients in forcing low-level winds and convergence in the tropics. *J. Atmos. Sci.*, *44*, 2418–2436. doi: 10.1175/1520-0469(1987)044⟨2418:OTROSS⟩2.0.CO;2

Liu, W. T., & Xie, X. (2002). Double intertropical convergence zones–A new look using scatterometer. *Geophys. Res. Lett.*, *29*, 2092.

Mace, G. G., & Zhang, Q. (2014). The cloudsat radar-lidar geometrical profile product (rl-geoprof): Updates, improvements, and selected results. *Journal of Geophysical Research: Atmospheres*, *119*(15), 9441-9462. Retrieved from `https://agupubs.onlinelibrary.wiley.com/doi/abs/10.1002/2013JD021374` doi: https://doi.org/10.1002/2013JD021374

Mahrt, L. J. (1972a). A numerical study of the influence of advective accelerations in an idealized, low-latitude, planetary boundary layer. *J. Atmos. Sci.*, *29*, 1477–1484. doi: 10.1175/1520-0469(1972)029⟨1477:ANSOTI⟩2.0.CO;2

Mahrt, L. J. (1972b). A numerical study of the influence of advective accelerations in an idealized, low-latitude, planetary boundary layer2. *J. Atmos. Sci.*, *29*, 1477–1484. doi: 10.1175/1520-0469(1972)029⟨1477:ANSOTI⟩2.0.CO;2

Mansbach, D. K., & Norris, J. R. (2007). Low-level cloud variability over the equatorial cold tongue in observations and models. *Journal of Climate*, *20*(8), 1555 - 1570. Retrieved from `https://journals.ametsoc.org/view/journals/clim/20/8/jcli4073.1.xml` doi: https://doi.org/10.1175/JCLI4073.1

McGauley, M., Zhang, C., & Bond, N. (2004). Large-scale characteristics of the atmospheric boundary layer in the eastern Pacific cold tongue-ITCZ region. *J. Climate*, *17*, 3907–3920. doi: 10.1175/1520-0442(2004)017⟨3907:LCOTAB⟩2.0.CO;2

Mechoso, C., Robertson, A., Barth, N., Davey, M., Delecluse, P., Gent, P., ... Tribbia, J. (1995). The seasonal cycle over the tropical Pacific in coupled ocean-atmosphere general circulation models. *Mon. Wea. Rev.*, *123*(9), 2825–2838. doi: 10.1175/1520-0493(1995)123⟨2825:TSCOTT⟩2.0.CO;2

Nam, C., Bony, S., Dufresne, J.-L., & Chepfer, H. (2012). The 'too few, too bright' tropical low-cloud problem in cmip5 models. *Geophysical Research Letters*, *39*(21). Retrieved from `https://agupubs.onlinelibrary.wiley.com/doi/abs/10.1029/2012GL053421` doi: https://doi.org/10.1029/2012GL053421

Philander, S. G. H., Gu, D., Lambert, G., Li, T., Halpern, D., Lau, N.-C., & Pacanowski, R. C. (1996). Why the ITCZ is mostly north of the equator.

J. Climate, *9*, 2958–2972. Retrieved from http://dx.doi.org/10.1175/1520-0442(1996)009<2958:WTIIMN>2.0.CO;2

Powell, M. D., Vickery, P. J., & Reinhold, T. A. (2003). Reduced drag coefficient for high wind speeds in tropical cyclones. *Nature*, *422*, 279–283. doi: 10.1038/nature01481

Raymond, D. J., Bretherton, C. S., & Molinari, J. (2006). Dynamics of the intertropical convergence zone of the east Pacific. *J. Atmos. Sci.*, *63*, 582–597. doi: 10.1175/JAS3642.1

Raymond, D. J., & Fuchs-Stone, v. (2021). Emergent Properties of Convection in OTREC and PREDICT. *J. Geophys. Res. Atmos.*, *126*(4), e2020JD033585. doi: https://doi.org/10.1029/2020JD033585

Sobel, A. H., & Neelin, J. D. (2006). The boundary layer contribution to intertropical convergence zones in the quasi-equilibrium tropical circulation model framework. *Theor. Comput. Fluid Dyn.*. doi: 10.1007/s00162-006-0033-y

Song, F., & Zhang, G. J. (2016). Effects of southeastern pacific sea surface temperature on the double-itcz bias in ncar cesm1. *Journal of Climate*, *29*(20), 7417 - 7433. Retrieved from https://journals.ametsoc.org/view/journals/clim/29/20/jcli-d-15-0852.1.xml doi: 10.1175/JCLI-D-15-0852.1

Stevens, B., Ackerman, A. S., Albrecht, B. A., Brown, A. R., Chlond, A., Cuxart, J., … Stevens, D. E. (2001). Simulations of trade wind cumuli under a strong inversion. *Journal of the Atmospheric Sciences*, *58*(14), 1870 - 1891. Retrieved from https://journals.ametsoc.org/view/journals/atsc/58/14/1520-0469_2001_058_1870_sotwcu_2.0.co_2.xml doi: 10.1175/1520-0469(2001)058⟨1870:SOTWCU⟩2.0.CO;2

Stevens, B., Brogniez, H., Kiemle, C., Lacour, J.-L., Crevoisier, C., & Kiliani, J. (2017). Structure and dynamical influence of water vapor in the lower tropical troposphere. *Surveys in Geophysics*, *38*, 1371–1397. Retrieved from https://doi.org/10.1007/s10712-017-9420-8 doi: 10.1007/s10712-017-9420-8

Tomas, R. A., Holton, J. R., & Webster, P. J. (1999). The influence of cross-equatorial pressure gradients on the location of near-equatorial convection. *Quart. J. Roy. Meteor. Soc.*, *125*, 1107–1127. doi: 10.1002/qj.1999.49712555603

Wallace, J. M., Mitchell, T. P., & Deser, C. (1989). The influence of sea-surface temperature on surface wind in the eastern equatorial pacific: Seasonal and interannual variability. *Journal of Climate*, *2*(12), 1492 - 1499. Retrieved from https://journals.ametsoc.org/view/journals/clim/2/12/1520-0442_1989_002_1492_tiosst_2_0_co_2.xml doi: 10.1175/1520-0442(1989)002⟨1492:TIOSST⟩2.0.CO;2

Woelfle, M. D., Bretherton, C. S., Hannay, C., & Neale, R. (2019). Evolution of the double-ITCZ bias through CESM2 development. *J. Adv. Model. Earth Syst.*, *11*(7), 1873–1893. doi: 10.1029/2019MS001647

Wood, R. (2012). Stratocumulus clouds. *Monthly Weather Review*, *140*(8), 2373 - 2423. Retrieved from https://journals.ametsoc.org/view/journals/mwre/140/8/mwr-d-11-00121.1.xml doi: 10.1175/MWR-D-11-00121.1

Xiang, B., Zhao, M., Held, I. M., & Golaz, J.-C. (2017). Predicting the severity of spurious "double ITCZ" problem in CMIP5 coupled models from AMIP simulations. *Geophys. Res. Lett.*, *44*(3), 1520–1527. Retrieved from https://agupubs.onlinelibrary.wiley.com/doi/abs/10.1002/2016GL071992 doi: 10.1002/2016GL071992

Xiang, B., Zhao, M., Ming, Y., Yu, W., & Kang, S. M. (2018). Contrasting impacts of radiative forcing in the southern ocean versus southern tropics on itcz position and energy transport in one gfdl climate model. *Journal of Climate*, *31*(14), 5609 - 5628. Retrieved from https://journals.ametsoc.org/view/journals/clim/31/14/jcli-d-17-0566.1.xml doi: 10.1175/JCLI-D-17-0566.1

Xie, S.-P., & Philander, S. G. H. (1994). A coupled ocean-atmosphere model of relevance to the itcz in the eastern pacific. *Tellus A: Dynamic Meteorology and Oceanography*, *46*(4), 340-350. Retrieved from https://doi.org/10.3402/tellusa.v46i4.15484 doi: 10.3402/tellusa.v46i4.15484

Yang, D. (2018a). Boundary layer diabatic processes, the virtual effect, and convective self-aggregation. *Journal of Advances in Modeling Earth Systems*, *10*(9), 2163-2176. Retrieved from https://agupubs.onlinelibrary.wiley.com/doi/abs/10.1029/2017MS001261 doi: https://doi.org/10.1029/2017MS001261

Yang, D. (2018b). Boundary layer height and buoyancy determine the horizontal scale of convective self-aggregation. *Journal of the Atmospheric Sciences*, *75*(2), 469 - 478. Retrieved from https://journals.ametsoc.org/view/journals/atsc/75/2/jas-d-17-0150.1.xml doi: https://doi.org/10.1175/JAS-D-17-0150.1

Zhang, C. (2001). Double ITCZs. *J. Geophys. Res.*, *106*, 11785–11792. doi: 10.1029/2001JD900046

Zhang, G. J., Song, X., & Wang, Y. (2019). The double itcz syndrome in gcms: A coupled feedback problem among convection, clouds, atmospheric and ocean circulations. *Atmospheric Research*, *229*, 255–268. Retrieved from https://www.sciencedirect.com/science/article/pii/S0169809518316788 doi: https://doi.org/10.1016/j.atmosres.2019.06.023

Zhang, M. H., Lin, W. Y., Klein, S. A., Bacmeister, J. T., Bony, S., Cederwall, R. T., … Zhang, J. H. (2005). Comparing clouds and their seasonal variations in 10 atmospheric general circulation models with satellite measurements. *Journal of Geophysical Research: Atmospheres*, *110*(D15). Retrieved from https://agupubs.onlinelibrary.wiley.com/doi/abs/10.1029/2004JD005021 doi: https://doi.org/10.1029/2004JD005021

Zhou, S., Huang, G., & Huang, P. (2020). Excessive itcz but negative sst biases in the tropical pacific simulated by cmip5/6 models: The role of the meridional pattern of sst bias. *Journal of Climate*, *33*(12), 5305 - 5316. Retrieved from https://journals.ametsoc.org/view/journals/clim/33/12/jcli-d-19-0922.1.xml doi: 10.1175/JCLI-D-19-0922.1

Figure 1.

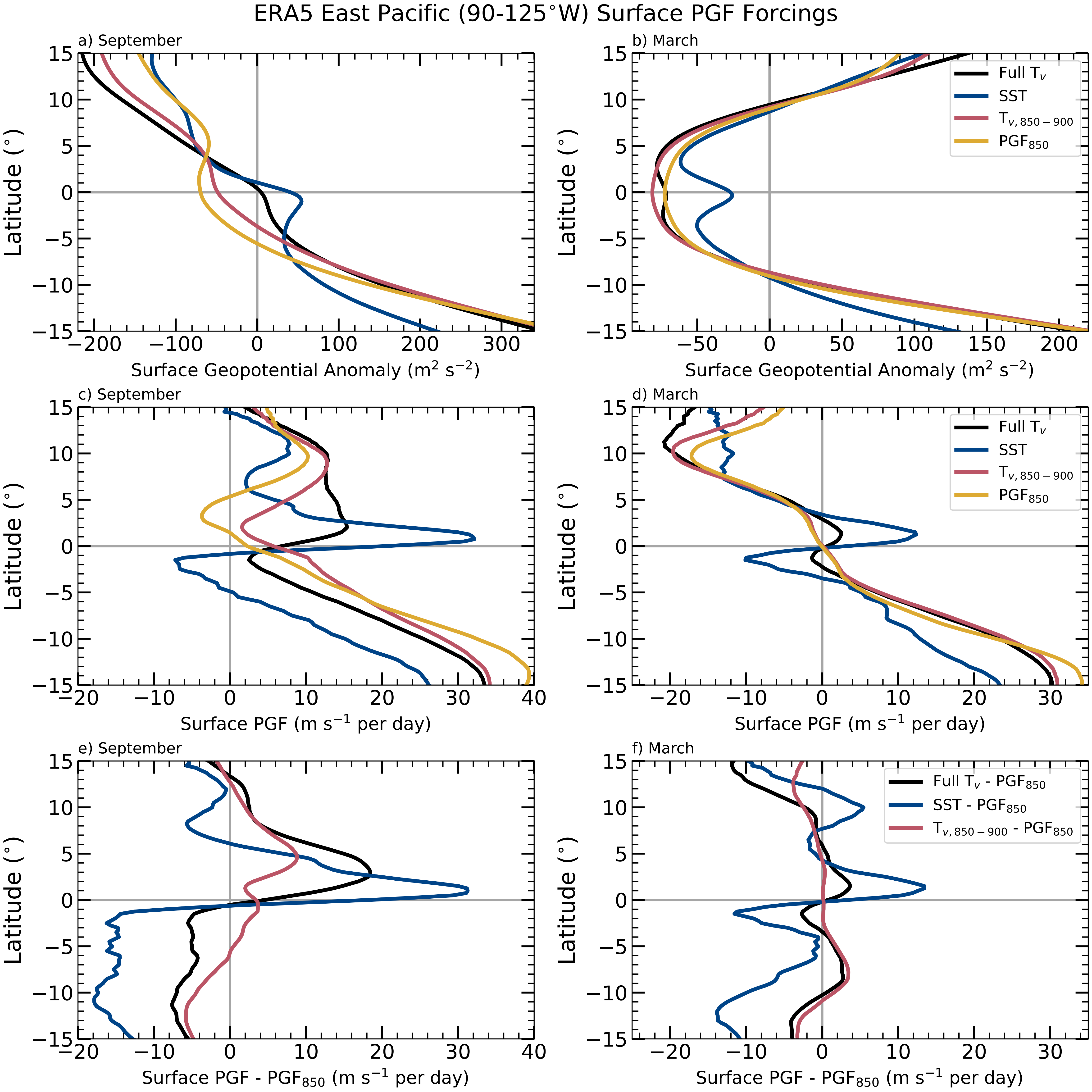

ERA5 East Pacific (90-125°W) Surface PGF Forcings
a) September
b) March
c) September
d) March
e) September
f) March
Latitude (°)
Surface Geopotential Anomaly (m^2 s^{-2})
Surface PGF (m s^{-1} per day)
Surface PGF - PGF$_{850}$ (m s^{-1} per day)
Full T$_v$
SST
T$_{v,850-900}$
PGF$_{850}$
Full T$_v$ - PGF$_{850}$
SST - PGF$_{850}$
T$_{v,850-900}$ - PGF$_{850}$

Figure 2.

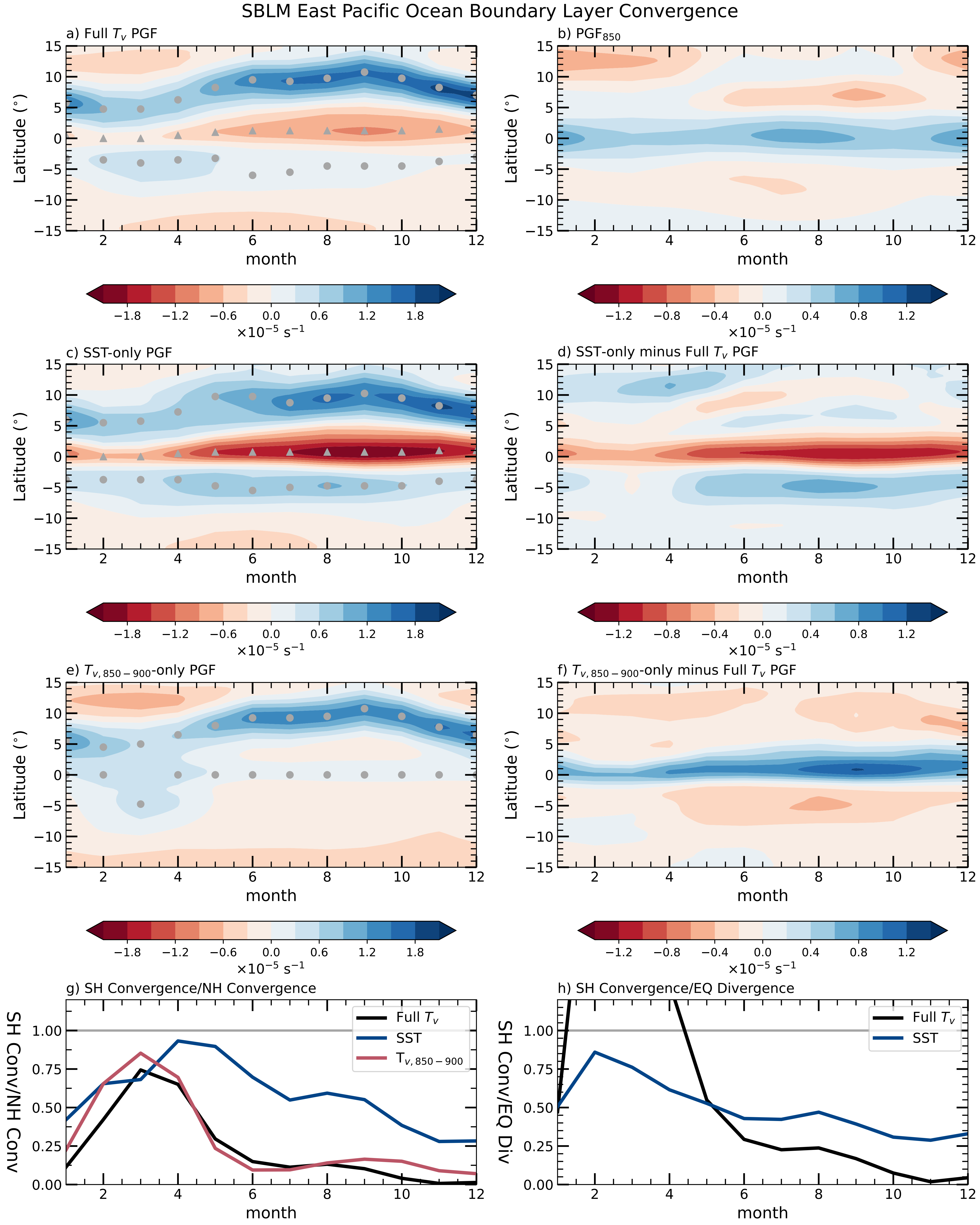
SBLM East Pacific Ocean Boundary Layer Convergence
a) Full T_v PGF
b) PGF_{850}
c) SST-only PGF
d) SST-only minus Full T_v PGF
e) $T_{v,850-900}$-only PGF
f) $T_{v,850-900}$-only minus Full T_v PGF
g) SH Convergence/NH Convergence
h) SH Convergence/EQ Divergence
Latitude (°)
month
$\times 10^{-5}$ s^{-1}
SH Conv/NH Conv
SH Conv/EQ Div
Full T_v
SST
$T_{v,850-900}$

Figure 3.

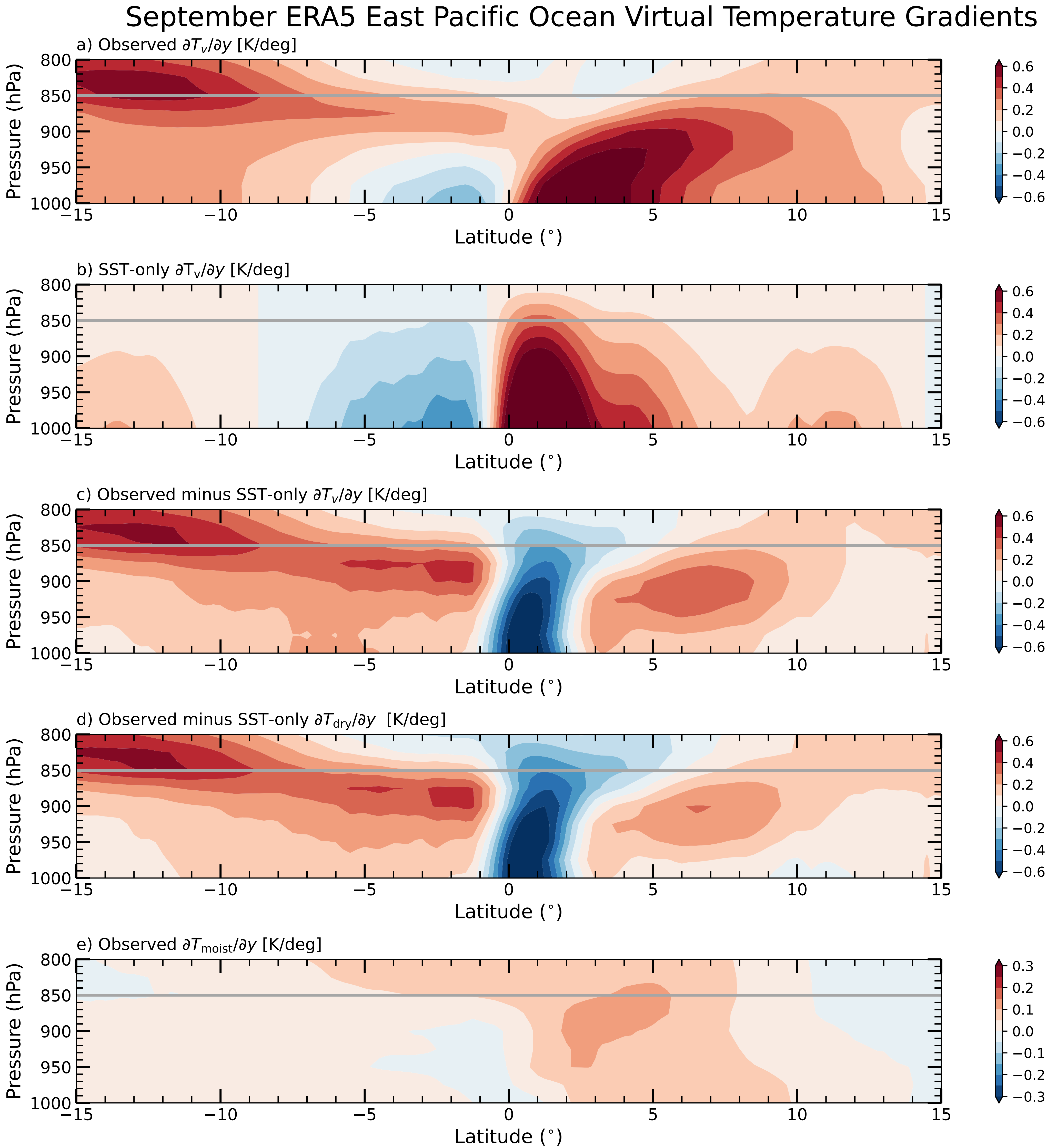
September ERA5 East Pacific Ocean Virtual Temperature Gradients
a) Observed $\partial T_v/\partial y$ [K/deg]
b) SST-only $\partial T_v/\partial y$ [K/deg]
c) Observed minus SST-only $\partial T_v/\partial y$ [K/deg]
d) Observed minus SST-only $\partial T_{dry}/\partial y$ [K/deg]
e) Observed $\partial T_{moist}/\partial y$ [K/deg]
Pressure (hPa)
Latitude (°)
800
850
900
950
1000
−15
−10
−5
0
5
10
15
0.6
0.4
0.2
0.0
−0.2
−0.4
−0.6
0.3
0.2
0.1
−0.1
−0.2
−0.3

Figure 4.

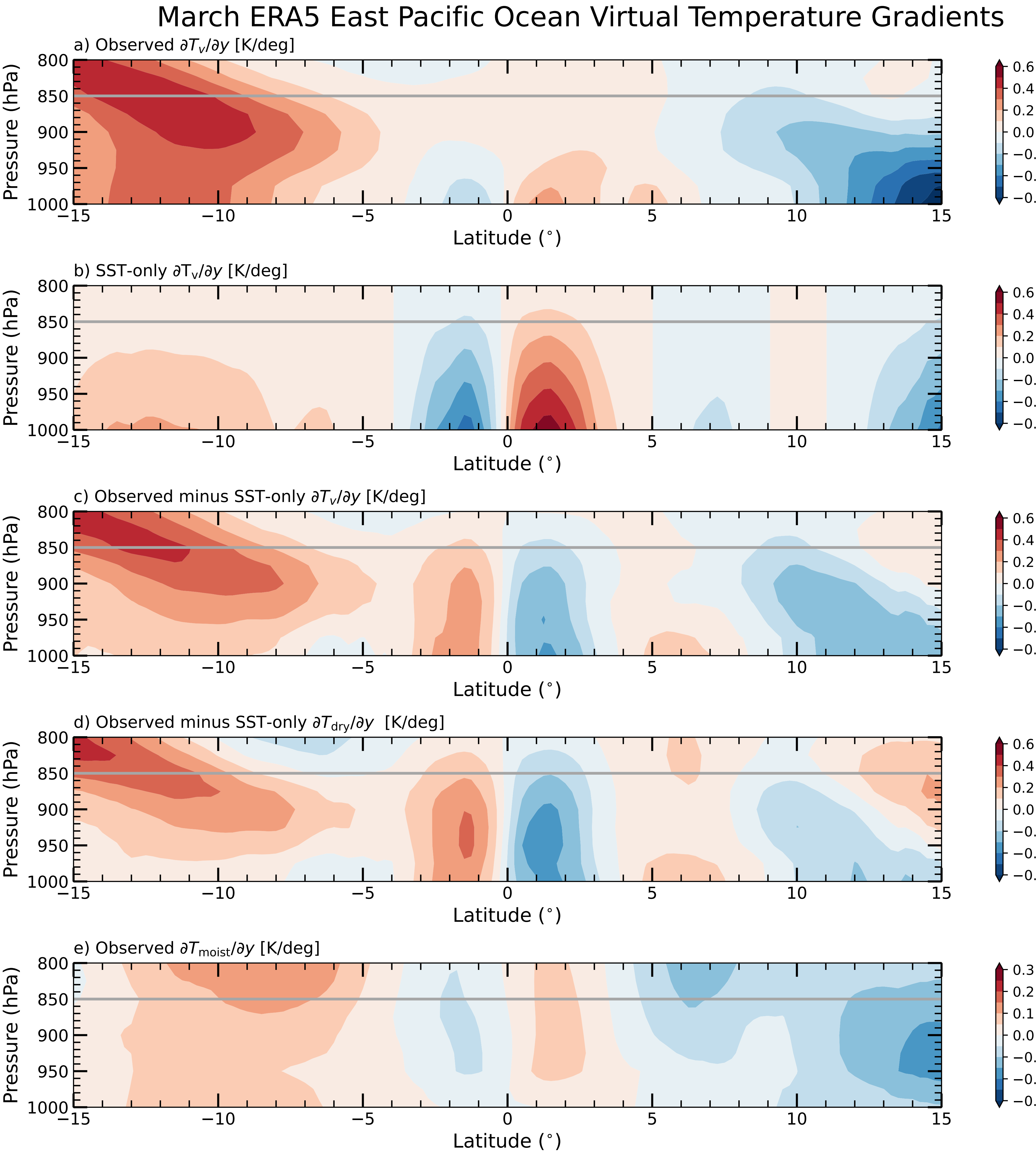
March ERA5 East Pacific Ocean Virtual Temperature Gradients
a) Observed $\partial T_v/\partial y$ [K/deg]
b) SST-only $\partial \mathrm{T_v}/\partial y$ [K/deg]
c) Observed minus SST-only $\partial T_v/\partial y$ [K/deg]
d) Observed minus SST-only $\partial T_{\mathrm{dry}}/\partial y$ [K/deg]
e) Observed $\partial T_{\mathrm{moist}}/\partial y$ [K/deg]
Pressure (hPa)
Latitude (°)
800
850
900
950
1000
−15
−10
−5
0
5
10
15
0.6
0.4
0.2
0.0
−0.2
−0.4
−0.6
0.3
0.2
0.1
−0.1
−0.2
−0.3

Figure 5.

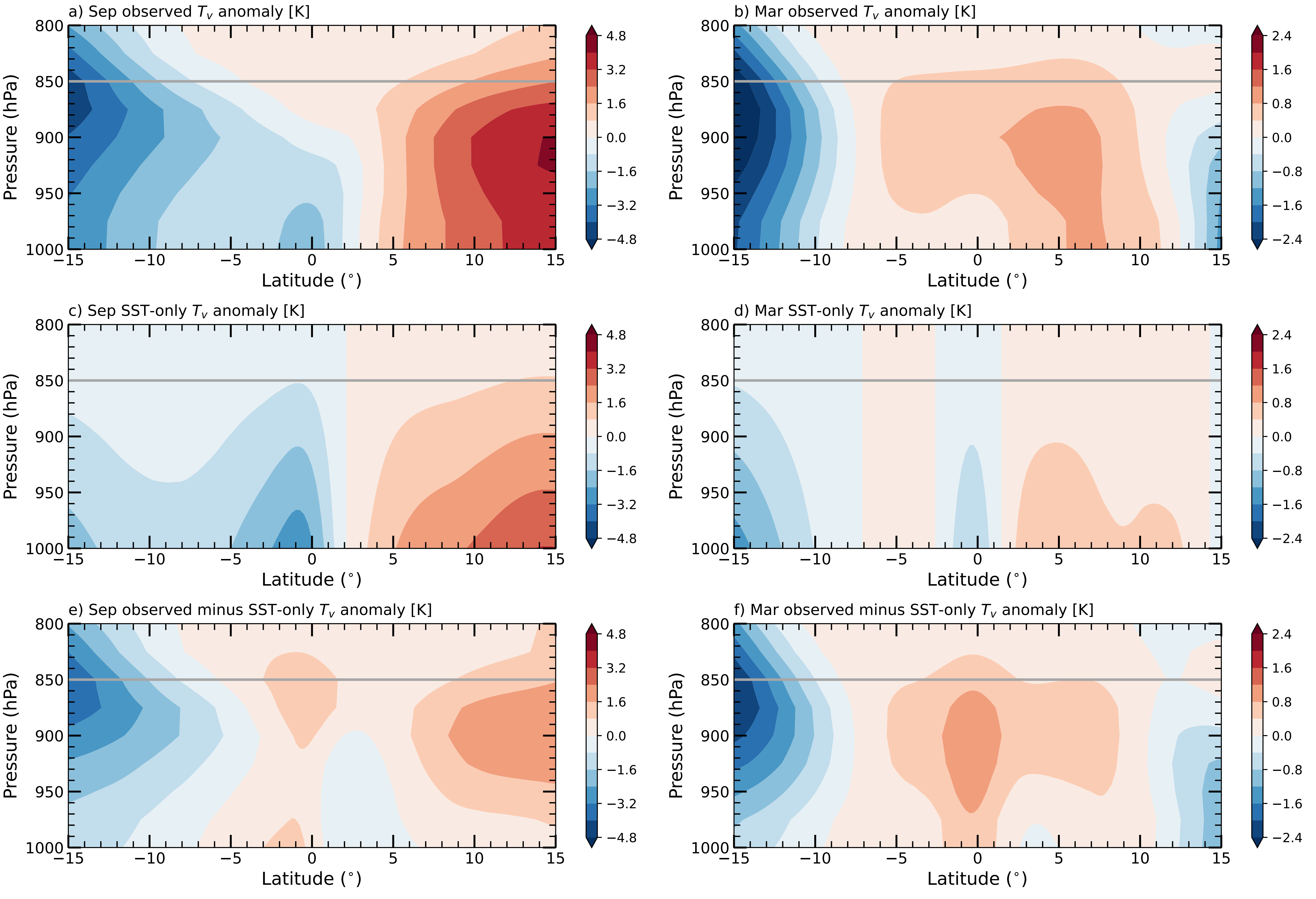

a) Sep observed T_v anomaly [K]
b) Mar observed T_v anomaly [K]
c) Sep SST-only T_v anomaly [K]
d) Mar SST-only T_v anomaly [K]
e) Sep observed minus SST-only T_v anomaly [K]
f) Mar observed minus SST-only T_v anomaly [K]
Pressure (hPa)
Latitude (°)
800
850
900
950
1000
−15
−10
−5
0
5
10
15
4.8
3.2
1.6
0.0
−1.6
−3.2
−4.8
2.4
1.6
0.8
0.0
−0.8
−1.6
−2.4

Figure 6.

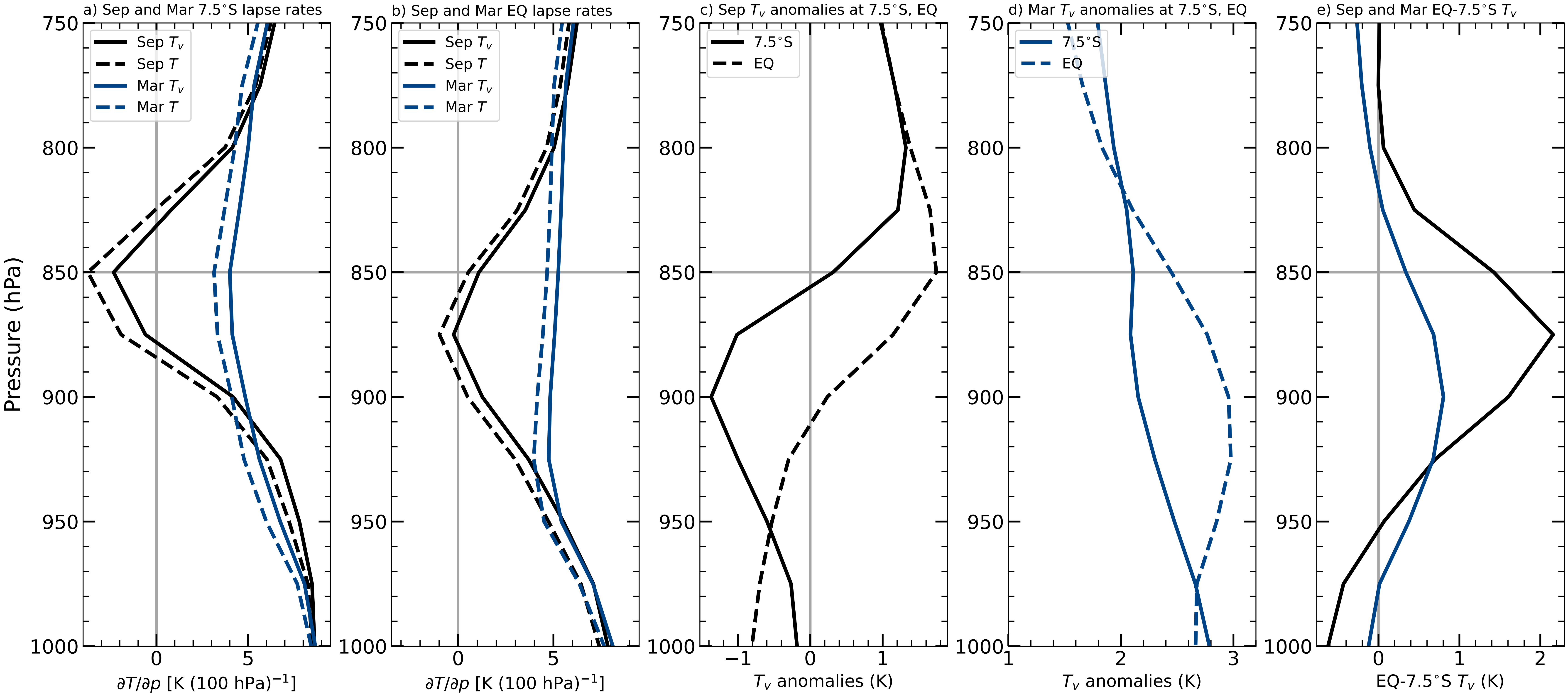

a) Sep and Mar 7.5°S lapse rates
b) Sep and Mar EQ lapse rates
c) Sep T_v anomalies at 7.5°S, EQ
d) Mar T_v anomalies at 7.5°S, EQ
e) Sep and Mar EQ-7.5°S T_v
Sep T_v
Sep T
Mar T_v
Mar T
7.5°S
EQ
Pressure (hPa)
750
800
850
900
950
1000
$\partial T/\partial p$ [K (100 hPa)$^{-1}$]
T_v anomalies (K)
EQ-7.5°S T_v (K)

Figure 7.

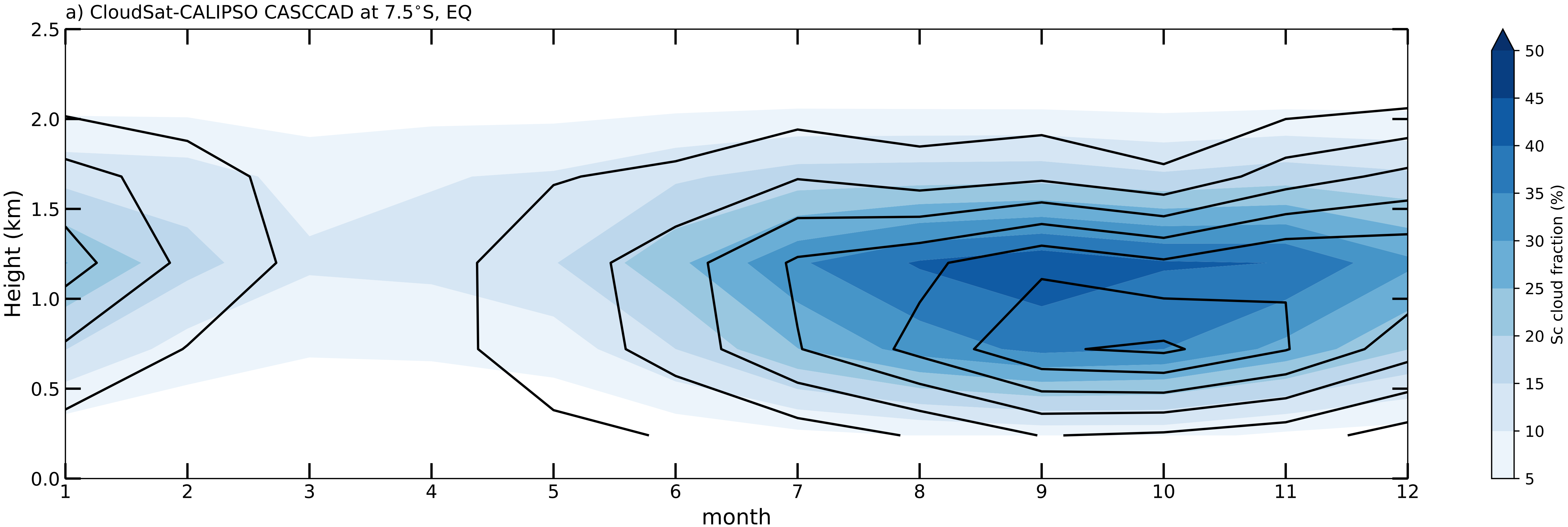

a) CloudSat-CALIPSO CASCCAD at 7.5°S, EQ
Height (km)
month
Sc cloud fraction (%)

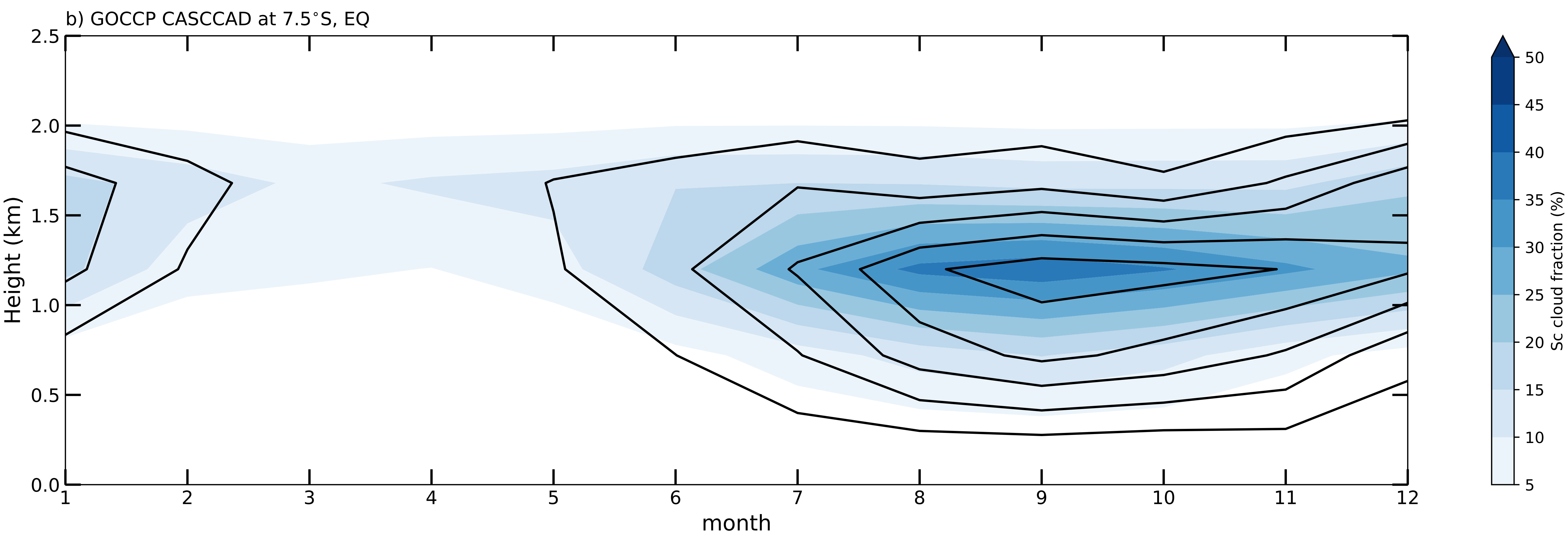

b) GOCCP CASCCAD at 7.5°S, EQ
Height (km)
month
Sc cloud fraction (%)

Figure 8.


3 km
1.5 km
0 km
COLD
Low clouds
ITCZ
WARM
Cold
tongue
25°S
20°S
10°S
EQUATOR
10°N
20°N
25°N